Long-term MAX-DOAS network observations of NO_2 in Russia and Asia (MADRAS) during 2007–2012: instrumentation, elucidation of climatology, and comparisons with OMI satellite observations and global model simulations

Y. Kanaya[1], H. Irie[1,*], H. Takashima[1,], H. Iwabuchi[1,***], H. Akimoto[1,****], K. Sudo[2], M. Gu[3], J. Chong[3], Y. J. Kim[3], H. Lee[3,*****], A. Li[4], F. Si[4], J. Xu[4], P-H. Xie[4], W- Q. Liu[4], A. Dzhola[5], O. Postylyakov[5], V. Ivanov[5,******], E. Grechko[5], S. Terpugova[6], and M. Panchenko[6]**

[1]Research Institute for Global Change, Japan Agency for Marine-Earth Science and Technology, Yokohama 2360001, Japan

[2]Nagoya University, Nagoya 4648601, Japan

[3]Gwangju Institute of Science and Technology (GIST), Gwangju 500712, Korea

[4]Anhui Institute of Optics and Fine Mechanics, Chinese Academy of Sciences, Hefei 230031, China

[5]A. M. Obukhov Institute of Atmospheric Physics, Russian Academy of Sciences, Moscow 119017, Russia

[6] V. E. Zuev Institute of Atmospheric Optics, Siberian Branch of the Russian Academy of Sciences, Tomsk 634021, Russia

[*]now at: Chiba University, Chiba 2638522, Japan

[**]now at: Fukuoka University, Fukuoka 8140180, Japan

[***]now at: Tohoku University, Sendai 9808578, Japan

[****]now at: Asia Center for Air Pollution Research, Niigata 9502144, Japan

[*****]now at: Pukyong National University, Pusan 608737, Korea

[******] now at: National Ozone Monitoring Research and Educational Center of Belarusian State University (NOMREC BSU), Minsk 220064, Belarus

Correspondence to: Y. Kanaya (yugo@jamstec.go.jp)

Abstract. We conducted long-term network observations using standardized Multi-Axis Differential optical absorption spectroscopy (MAX-DOAS) instruments in Russia and ASia (MADRAS) from 2007 onwards and made the first synthetic data analysis. At seven locations (Cape Hedo, Fukue, and Yokosuka in Japan, Hefei in China, Gwangju in Korea, and Tomsk and Zvenigorod in Russia) with different levels of pollution, we obtained 80,927 retrievals of tropospheric NO_2 vertical column density (TropoNO2VCD) and aerosol optical depth (AOD). In the technique, the optimal estimation of the TropoNO2VCD and its profile was performed using aerosol information derived from O_4 absorbances simultaneously observed at 460–490 nm. This large data set was used to analyze NO_2 climatology systematically, including temporal variations from the seasonal to the diurnal scale. The results were compared with Ozone Monitoring Instrument (OMI) satellite observations and global model simulations. Two NO_2 retrievals of OMI satellite data (NASA ver. 2.1 and Dutch OMI NO_2 (DOMINO) ver. 2.0) generally showed close correlations with those derived from MAX-DOAS observations, but had low biases up to ~50%. The bias was distinct when NO_2 was abundantly present near the surface and when the AOD was high, suggesting a possibility of incomplete accounting of NO_2 near the surface under relatively high aerosol conditions for the satellite observations. Except for constant biases, the satellite observations showed nearly perfect seasonal agreement with MAX-DOAS observations, suggesting that the analysis of seasonal features of the satellite data were robust. Weekend reduction in the TropoNO2VCD found at Yokosuka and Gwangju was absent at Hefei, implying that the major sources had different weekly variation patterns. While the TropoNO2VCD generally decreased during the midday hours, it exceptionally increased at urban/suburban locations (Yokosuka, Gwangju, and Hefei) during winter. A global chemical transport model, MIROC-ESM-CHEM, was validated for the first time with respect to background NO_2 column densities during summer at Cape Hedo and Fukue in the clean marine atmosphere.

1 Introduction

Nitrogen oxides (NO_x), i.e., NO and NO_2, are key chemical species in driving tropospheric photochemistry, and they participate in the mechanisms used to explain local to global air pollution. They are originally emitted or produced from natural (soil and lightning) and anthropogenic sources, and are strongly involved in the chain reactions forming tropospheric ozone (O_3). The reaction of NO with peroxy radicals (HO_2 and organic peroxy radicals, RO_2) produces NO_2, resulting in net production of O_3 via subsequent photolysis of NO_2. This reaction simultaneously recycles OH radicals, which determine the atmospheric oxidative capacity, and this sustains the concentration levels of peroxy radicals. Under heavily polluted conditions, NO_2 provides a major pathway for loss of OH, nonlinearly controlling the oxidative capacity. The deposition of nitric acid, produced from the reaction of OH + NO_2, and of nitrate aerosols, normally formed by gas-to-particle partition of nitric acid, on the Earth's surface fertilizes terrestrial and marine ecosystems (Duce et al., 2008), as well as causing acidification. Knowledge of global and regional distributions of NO_2, their temporal variations, and the underlying mechanisms therefore provides a firm basis for investigations of multi-scale air pollution and the nitrogen cycle.

Recent orbiting satellite sensors have enabled monitoring of the tropospheric NO_2 vertical column density (TropoNO2VCD) from the regional to the global scale (e.g., Burrows et al., 1999). Past studies have shown that large spatial inhomogeneity, strong seasonal variations, and long-term trends are present (e.g., Richter et al., 2005; Boesma et al., 2007; Martin et al., 2006; van der A et al., 2008). In Asia, particularly Central East China (110–122° E, 30–40° N), the highest TropoNO2VCD values in the world have been recorded in recent years. Compared with the aerosol optical depth (AOD), another observable parameter from satellite sensors, for which various types of ground-based long-term monitoring networks such as AERONET (AErosol RObotic NETwork, Holben et al., 2001), SKYNET (http://atmos.cr.chiba-u.ac.jp/), and light detection and ranging (lidar) networks can provide a firm basis for validation,

TropoNO2VCD has been evaluated with independent observations relatively infrequently. It is strategically important to certify satellite observations through comparisons with qualified observations regarded as ground truth; the verified spatial distributions or temporal variations are then used for further analysis.

In the past, aircraft-based in situ observations (Bucsela et al., 2008; Celarier et al., 2008), ground-based direct-sun Brewer measurements (Wenig et al., 2008), zenith DOAS (differential optical absorption spectroscopy) (Chen et al., 2009), lidar systems (Hains et al., 2010), urban air quality monitoring networks (Boersma et al., 2008), and combinations with model simulations (Lamsal et al., 2010) have been used for validation of satellite-based observations of tropospheric NO_2. Multi-axis DOAS (MAX-DOAS) observations (Hönninger et al., 2004; Wittrock et al., 2004; Sinreich et al., 2005) have also been proven to provide suitable columnar data for validation of satellite observations. In the past, MAX-DOAS observations over relatively short periods have been used for the validation of satellite-based observations of tropospheric NO_2 (e.g., Heue et al., 2005, Brinksma et al., 2008, Celarier et al., 2008, Irie et al., 2008a, 2009a; Hains et al., 2010; Shaiganfar et al., 2011; Peters et al., 2012). For more systematic validation, a long-term ground-based monitoring network for NO_2 is highly desirable.

So far, several MAX-DOAS network observations have been reported. Two of these, established at an early stage, are the BREDOM (Bremian DOAS network for atmospheric measurements) network, including Bremen, Ny-Ålesund, Nairobi, Mérida, and Heraklion (e.g., Wittrock et al., 2004), and a network maintained by the Belgian Institute for Space Aeronomy (BIRA-IASB) (http://uv-vis.aeronomie.be/groundbased/), including Harestua, Jungfraujoch, Observatoire de Haute-Provence (OHP), Reunion Island, Beijing, and Uccle (e.g., Clémer et al., 2010). At these sites, high-quality spectroscopy is performed using high-grade spectrometers and charged-couple device (CCD) detectors, enabling retrievals of weak absorbers (e.g., BrO) in the troposphere and stratosphere. Valks et al. (2011) used

MAX-DOAS observations of TropoNO2VCD at OHP for 4 years to validate Global Ozone Monitoring Experiment-2 (GOME-2) satellite observations. Hendrick et al. (2013) studied temporal variations in NO_2 and HONO derived from MAX-DOAS observations for 4 years in and near Beijing.

As a Global Earth Observation System of Systems (GEOSS)-related project funded by the Japanese government during FY2006–2010, we established a long-term NO_2-monitoring network based on MAX-DOAS over Russia and Asia (MADRAS). This paper provides an overview of these network observations. Our strategy is to use a relatively low-cost miniature spectrometer to obtain spectra of compromised, but still sufficient, quality. A similar approach was used for a network for monitoring volcano plumes (Galle et al., 2010). Recently, the Max Planck Institute reported long-term observations of NO_2 in Beijing using a low-cost MAX-DOAS instrument and comparisons of the data with satellite observations (e.g., Ma et al., 2013). Heidelberg University (Ulrich Platt, personal communication, 2011) operates about 10 instruments, and the Anhui Institute of Optics and Fine Mechanics (AIOFM) runs more than 10 instruments within China (Wenqing Liu, personal communication, 2011), using a similar concept.

A major purpose of our network observations is to retrieve TropoNO2VCDs (and their vertical profiles) in the daytime to validate satellite observations at several key locations with different levels of air pollution, i.e., at Yokosuka, Cape Hedo, and Fukue (Japan), Gwangju (Korea), Hefei (China), and Zvenigorod and Tomsk (Russia). In addition, we aim to observe diurnal variations and vertical distributions of NO_2, beyond the capabilities of current satellite sensors on sun-synchronous orbits with fixed local time observations. We also aim to validate tropospheric chemical transport model simulations using the long-term record.

In this paper, we describe instrumental aspects of the network observations, features of temporal variations in the retrieved TropoNO2VCD data during 2007–2012 (for 3 to more than 5 years of observations for each site), and comparisons with Ozone Monitoring

Instrument (OMI) satellite observations and global model simulations. The instruments used at the individual sites were standardized so that the basic optical components used were the same. The obtained spectra were processed centrally to maintain homogeneous data quality over the sites. Temporal variations from diurnal, weekly, seasonal, to multi-year scales were investigated, and compared with satellite observations wherever possible.

2 Experimental

2.1 Instrumentation

The MAX-DOAS instruments deployed at our network sites consisted of a light-receiving part and a miniature spectrometer connected by a bundle optical fiber cable (Fig. 1). The spectrometers used were USB4000 (Ocean Optics, Dunedin, FL, USA) equipped with a linear array of CCD detectors with 3648 pixels (TCD1304AP; Toshiba, Tokyo, Japan), except for the #1 instrument at Fukue, which was used for only 2 months (see Table 1), where another miniature spectrometer (BTC111; B&W TEK Inc., Newark, DE, USA) was used. The light-receiving part incorporated a flat rectangular mirror, with a 45° incidence angle, located in a weather-shielding quartz tube cap, and a telescope with a single plano-convex quartz lens of diameter 25 mm and a focal length of 40 mm. The telescope was coupled with an optical bundle fiber cable (length 1 m or 5 m) via an SMA (subminiature version A) connector, which consisted of seven cores (each with a diameter of 100 μm and a numerical aperture of 0.22). The cores formed a circle at the telescope side end and were aligned vertically at the exit, to fit to the slit shape of the spectrometer. The telescope restricted the field of view angle to less than 1°. The field of view angle was tested by introducing light into the fiber retrospectively from the exit side, and the divergence of the light after exiting the telescope was evaluated.

The rectangular mirror was rotated every 5 min to introduce scattered sunlight from the sky, with sequential elevation angles of 3, 5, 10, 20, 30, and 90°, to the spectrometer through the telescope and the fiber bundle. One cycle of observations at six elevation angles (with

integration for 5 min for each) took 30 min. The cycle was repeated on a 24-h basis. The spectrometer integration time was fixed at a value between 100 and 400 ms during the day and night. The integration time changed seasonally so that the maximum signal level reached the middle range (between 20,000 and 40,000) of the full dynamic range of the 16-bit A/D converter (2^{16} = 65,536). A spectrum with a customized integration time was averaged over 250–600 integration times so that a single average spectrum was recorded every minute.

The USB4000 spectrometers used a standard grating (#5, a holographic grating for UV, with a groove density of 1200). The linear array CCD detector used the manufacturer's upgraded quartz window with UV transmittance and a cylindrical lens to enhance the efficiency. The slit width was generally 25 μm, except for the instrument installed at Cape Hedo, which had a slit width of 10 μm. The spectrometers were customized so that a wavelength range from 230 to 560 nm was covered and a wavelength resolution below 0.7 nm in full-width at half-maximum (FWHM) was attained at the 407.783-nm mercury line. The resulting wavelength resolution in the 460–490 nm range, used for the analysis of NO_2 and O_4 in this study, was observed to be between 0.4 and 0.7 nm. The spectrometer was further customized to improve coupling to the fiber cable: a key lock, normally used to reproduce the angular position of the linearly aligned fiber cores at the exit of the bundle cable (within the SMA connector) with respect to the slit vertically oriented at the spectrometer, was removed and the connection was manually optimized in the rotational direction. The distance from the fiber end to the spectrometer slit was simultaneously optimized by inserting thin nylon spacers into the bottom space of the ferrule of the SMA connector at the exit end of the fiber. Thus, in addition to wavelength resolution, the spectral symmetry (determining the slit function shape) was optimized at a mercury line (407.783 nm) for each instrument before installation. The original distance between the fiber end and the slit determined by the manufacturer was often too short to optimize the spectral symmetry, although the signal intensity was higher there than that at our optimized position.

Single-notch filters at 405, 442, 488, and 355 nm (NF03-405E-25, NF01-442U-25, NF03-488E-25; Semrock Inc., Rochester, NY, USA) with a blocking optical depth (OD) > 6 and FWHM in the range of 9–14 nm, and a 355-nm notch-filter (Edmund Optics, Barrington, NJ, USA) with a blocking OD > 4 and FWHM of 18 nm, were used for stray-light characterization of the instrument. For typical daylight conditions, the stray light levels were estimated to be only 0.6–1.0% of the daylight signal levels at each wavelength.

The elevation angles need to be absolutely accurate. The base plate of the light-receiving unit, to which the central axis of the telescope was parallel, was first set to be horizontal, using a horizontal level embedded in the base plate (Fig. 2). Subsequently, the angular position of the reflecting mirror at elevation angle = 0° was carefully adjusted. A stepping motor (with an angle step of 0.038°), used for controlling the mirror angle, was equipped with an optical angular position sensor, with which the zero position was first roughly determined. Then, an additional offset angle (at a resolution of 0.1°) with respect to the sensor position was precisely adjusted until the reflecting mirror became fully horizontal. The offset angle thus determined was registered in the initial file of the software for the mirror rotation and was activated all the time. In this procedure, we used a second horizontal level (Fig. 2) embedded in a plate holding the reflecting mirror at a perpendicular angle. The level was easily seen from the top of the instrument through the quartz cap, facilitating setup in the field. All the elevation angles used for the observations were determined in this way relative to the zero position initially set at installation. The long-term drift (over more than 1 year) of the zero position was typically less than 0.2°.

A laptop computer was used to control the mirror rotation and to collect all the spectra and house-keeping information (e.g., temperature control). A small fan was present beneath the quartz tube cap to avoid sedimentation of large aerosol particles on the surface of the cap, to remove small water droplets/snowflakes, and to reduce the possibility of small animals (e.g., spiders) interfering with the observations.

2.2 Observation sites

The instruments were deployed at seven locations (Figs. 3 and 4, Table 1): at Cape Hedo, Okinawa Island, southwest of Japan, in March 2007, at Yokosuka, Japan in April 2007, at Gwangju, Korea in February 2008, at Hefei, Anhui Province, China in March 2008, at Zvenigorod, Russia in October 2008, at Tomsk, Russiain January 2009, and at Fukue Island, Nagasaki Prefecture, west of Japan in February 2009. The geographic coordinates, altitudes, and the azimuth angles of the line of sight for each observation site are listed in Table 1. The Yokosuka site (about 30 km south of Tokyo) is located within an industrialized area that extends in the north–south direction along Tokyo Bay in the Kanto Plain. Cape Hedo is a remote site, located in the northern-most part of subtropical Okinawa Island (Takami et al., 2007; Kanaya et al., 2001), and is distant from major cites (40 km from Nago, population 60,000 and 100 km from Naha, population 320,000). For these two sites, five-fold optical axes were prepared for simultaneous observations at different elevation angles during intensive campaign periods. Under normal long-term operation, however, only a single telescope was used and the elevation angles were sequentially scanned. Gwangju site at the Gwangju Institute of Science and Technology is 8 km north-northwest of the Gwangju city center (population 1.4 million). The Hefei site is in the campus of AIOFM, about 10 km northwest of the Hefei city center (population 4.4 million). The Gwangju and Hefei sites are regarded as suburban sites. The Zvenigorod Research Station, affiliated to the Institute of Atmospheric Physics, Russian Academy of Sciences (Yurganov et al., 2010), is located in a rural area ~50 km west of Moscow, whose population is ~10.5 million. The observatory is registered as a Network Detection of Atmospheric Composition Change site with respect to stratospheric NO_2 observations. The observations at Tomsk took place in the campus of the Institute of Atmospheric Optics, Siberian Branch of the Russian Academy of Sciences. The site is ~5 km east of the Tomsk city center, whose population is 520,000. For the two instruments located in Russia, the heat insulation was strengthened to tolerate low ambient

temperatures during winter (between –20 and –40 °C). The data from Tomsk are still being evaluated, and will not be used in the following discussions. The Fukue site is remote, away from major cities (e.g., 100 km from Nagasaki, population 440,000). The differences of the local time (LT) from UTC are +9 h for Cape Hedo, Yokosuka, Fukue and Gwangju, +8 h for Hefei, and +4 h for Zvenigorod.

At each site, the light-receiving unit of the MAX-DOAS instrument was located on the rooftop of single to five-story building. Three types of deployment layout were used with respect to the spectrometer (type A, B, and C, see Table 1). For type A and B, the spectrometer was located indoors in a customized thermoelectrically controlled refrigerator (type A) or in a temperature stabilized case (type B). The controlled temperature was 20 or 25 °C for type A and 40 °C for type B for all seasons. For type C, the spectrometer was located outdoors in a light-receiving unit and its temperature was controlled to seasonally-changing levels (25 or 30 °C in winter and 35 or 45 °C in summer). The precise temperature stabilization within ±0.2 °C (using KT4; Panasonic, Kadoma, Japan) on a 24-h basis was important for the purpose of subtracting the dark spectrum measured during the night from the daytime spectra. A large part of the pixel-to-pixel pattern variability in the dark spectrum was constant over time, as long as the temperature was constant. For example, in the case of 38 °C, the pixel-to-pixel variability was as much as 96 digits as a standard deviation (1σ), for a spectrum obtained with an integration time of 100 ms averaged 600 times. However, after subtraction of the averaged dark "pattern" spectrum, recorded during the night-time, the random noise (pixel-to-pixel) was as small as 2–3.5. A signal-to-noise ratio of the order of 10^4 was therefore expected, which was typically required to analyze weak absorptions (<0.1%) quantitatively. Temperature stabilization was also important for keeping the wavelength shift constant over a long time period.

2.3 Retrieval algorithms

The recorded spectra were processed centrally so that the network observations produced data of homogeneous quality. The retrieval algorithm was similar to that used for JM1 (Irie et al., 2011), but (1) QDOAS software ver. 2.00 (http://uv-vis.aeronomie.be/software/QDOAS/, Fayt and Roozendael, 2012) was used for DOAS analysis, and (2) a newly coded Fortran program was used for subsequent conversion of the differential slant column densities (ΔSCDs) to vertical quantities. The basic flow of the analysis was similar to that used previously (Irie et al., 2008a,b, 2009a). Briefly, the measured spectra of scattered sunlight in the range of 460–490 nm at low elevation angles were analyzed, using the DOAS technique (Platt, 1994), to retrieve the ΔSCDs of oxygen collision complexes (O_2–O_2 or O_4) and NO_2 with respect to the reference spectrum obtained at the highest elevation angle (90° or 70°). A reference spectrum was derived by interpolating two spectra measured within 30 min before and after the off-axis measurement. The absorption by gaseous species, i.e., O_4, NO_2, O_3, and H_2O, and the Ring effect were taken into account. The absorption cross-sections used were those reported by Herman et al. (http://spectrolab.aeronomie.be/o2.htm) for O_4, Vandaele et al. (1996) for NO_2 at 298 K, Bogumil et al. (2003) for O_3 at 223 K, and Rothman et al. (2003) for H_2O. The cross-sections of O_4 were increased by a factor of 1.25, following Clémer et al. (2010). A polynomial degree of three was used to fit the continuum. Typical residuals of spectral fitting were in the range of (5–20) × 10^{-4} for clear midday periods, but they increased in the early morning and late evening.

The O_4 ΔSCD values were next converted to the AODs and vertical profiles of the aerosol extinction coefficients, using the optimal estimation method (OEM) developed by Rodgers (2000). The measurement vector consisted of five O_4 ΔSCD values observed at low elevation angles. The state vector consisted of the AOD and three parameters (f_1, f_2, and f_3) determining the vertical profiles, with which the partial optical depths for the altitude ranges 0–1, 1–2, and 2–3 km were expressed as f_1 × AOD, $(1 - f_1) \times f_2 \times$ AOD, and $(1 - f_1) \times (1 - f_2) \times f_3 \times$ AOD, respectively (see Irie et al., 2008b). The a priori values and the errors in the AOD, f_1, f_2, and f_3

were chosen to be 0.21 ± 3.0, 0.60 ± 0.05, 0.80 ± 0.03, and 0.80 ± 0.03, respectively. A lookup table of box air mass factors (A_{box}), which characterized the ratio of the partial slant to the vertical columns for a given layer, was created using a three-dimensional Monte Carlo radiative transfer model, MCARaTS (Iwabuchi, 2006). A_{box} calculations using MCARaTS have been validated through comparisons with other radiative transfer models (Wagner et al., 2007). An optimal aerosol (and A_{box}) profile scenario that accounted for the O_4 ΔSCD values measured at all elevation angles was determined.

Using the A_{box} profiles and an iterative inversion method similar to that used for aerosol retrieval, a set of NO_2 ΔSCD values for low elevation angles (as the measurement vector) was then converted to a tropospheric VCD and a vertical profile of NO_2 using an OEM. The state vector included TropoNO2VCD, and the partial fraction parameters v_1, v_2, and v_3, with which the partial NO_2 VCDs in the altitude ranges 0–1, 1–2, and 2–3 km were expressed as TropoNO2VCD × v_1, TropoNO2VCD × (1 − v_1) × v_2, and TropoNO2VCD × (1 − v_1) × (1 − v_2) × v_3, respectively. The a priori values for TropoNO2VCD, v_1, v_2, and v_3 were selected to be 20% of the largest ΔSCD values for NO_2, 0.60 ± 0.05, 0.80 ± 0.03, and 0.80 ± 0.03, respectively. The NO_2 ΔSCD determinations using an instrument of the same design were validated during the CINDI 2009 (Cabauw Intercomparison Campaign of Nitrogen Dioxide measuring Instruments) campaign performed at Cabauw, the Netherlands, during June–July 2009 (Roscoe et al., 2010; Piters et al., 2012). The compatibility of the TropoNO2VCD data with those derived using the JM1 algorithm (Irie et al., 2011) was also confirmed.

Takashima et al. (2009) established an original cloud-screening method for studying aerosols at Cape Hedo using a combination of the MAX-DOAS color index (defined as the ratio of the intensities at 500 and 380 nm) and the relative humidity, derived from H_2O retrieved from the MAX-DOAS analysis. However, for the retrieval of NO_2, which is the main target of this study, critical cloud screening using the color index was not applied, because the NO_2 state would be retrieved properly as long as the optical path length was

313 determined correctly. It should also be noted that even without such screening using the color
314 index, a large fraction of cloudy cases was eliminated in advance, as the observed O_4 ΔSCD
315 values at five elevation angles were irregularly distributed and were not well fitted. See the
316 supplementary material for details of cloud screening using the color index applied for the
317 evaluation of the retrieved aerosol quantities.

318 Error estimation methodologies have been reported for random and systematic uncertainties
319 in aerosol retrievals (Irie et al., 2008a; Takashima et al., 2009). The overall uncertainty in the
320 AOD was estimated from our past comparisons with existing methods (sky radiometer and
321 Mie lidar) to be 30%. The method used to calculate random and systematic uncertainties in
322 TropoNO2VCD has been described elsewhere (Irie et al., 2009a, 2011). The random
323 uncertainty was estimated to be 10%, based on the residuals in the ΔSCD fitting. The
324 systematic error was estimated to be 14%, to which the uncertainties in the AOD and in the
325 A_{box} contributed by similar degree. The combined total uncertainty was typically 17%.
326 Takashima et al. (2011, 2012) reported that similar instruments had detection limits for NO_2
327 mixing ratios of <0.2 ppb at an altitude of 0–1 km, corresponding to a minimum detectable
328 TropoNO2VCD of $<5 \times 10^{14}$ molecules cm^{-2}.

329 Figure 5 demonstrates the performance of our retrievals for selected morning hours
330 [0800–0900 (8 h) or 0900–1000 (9 h) LT], and afternoon hours [1500–1600 (15 h) or
331 1600–1700 (16 h) LT] in June at three locations (Zvenigorod, Hefei, and Yokosuka). The O_4
332 ΔSCD values (Figs. 5a–c) showed negative dependences on the elevation angles, and they
333 were well fitted using the OEM. The low O_4 ΔSCD values at Hefei at all elevation angles (Fig.
334 5b) were explained by the presence of dense aerosols. The O_4 ΔSCD values in the afternoon
335 were higher at Hefei (Fig. 5b) and Yokosuka (Fig. 5c), and lower at Zvenigorod (Fig. 5a), than
336 those in the morning; this was mainly explained by differences among the relative azimuth
337 angles of observation. The retrieved AOD values were similar for the morning and afternoon
338 at all the sites. The NO_2 ΔSCD values were higher in the morning than in the afternoon in all

cases (Figs. 5d–f), because NO_2 was more abundant in the morning. At Zvenigorod and Hefei, the NO_2 ΔSCD values showed a stronger dependence on the elevation angle in the morning than in the afternoon, resulting in steeper vertical profiles (and higher v_1 values) in the morning (Figs. 5g and h). At Yokosuka, the dependence of the NO_2 ΔSCD values on elevation angle did not greatly change from the morning to the afternoon, and therefore the v_1 values and the vertical profiles of NO_2 were almost unchanged diurnally. This could be explained by continuous NO_x emissions from nearby sources at Yokosuka, sustaining a relatively steep vertical gradient at all times. In contrast, the less steep vertical gradients in NO_2 up to 2 km at Zvenigorod and Hefei in the afternoon could be explained by the fact that nearby sources were less important, and that the continental boundary layer height became thicker in the afternoon during summer. The degrees of freedom of the signal typically exceeded two during the daytime periods between the morning and afternoon hours studied here.

The final products of our retrieval were TropoNO2VCDs, AODs, vertical profiles of NO_2 and extinction coefficients, with a resolution of 1 km (up to 3 km) at a time resolution of 30 min during daytime. Careful quality control of the data was applied to remove cases with wrong mirror operations, power blackouts, shifts in the dark spectra as a result of changes in integration time and temperature settings, large residuals in the spectral fittings, malfunction in the temperature control, and saturated signal levels.

2.4 OMI satellite data products for comparison

In this section OMI satellite data products of TropoNO2VCD, to be compared with our MAX-DOAS products in section 3.1, are summarized. The OMI is a UV/vis nadir viewing spectrometer on the National Aeronautics and Space Administration (NASA) Aura satellite on a sun synchronous orbit launched in 2004. An OMI pixel size is 13 × 24 km^2 or larger. We used two different products, i.e., one derived from the algorithm developed by the NASA and the other from the algorithm (Dutch OMI NO_2 (DOMINO)) developed by Koninklijk Nederlands Meteorologisch Instituut. The NASA data set was the ver. 2.1 release of the

gridded OMNO2d daily level 3 products (OMNO2d.003), with cloud screening at 30%, at a resolution of 0.25° × 0.25°, available from the NASA Giovanni website (http://gdata1.sci.gsfc.nasa.gov/daac-bin/G3/gui.cgi?instance_id=omi; Bucsela et al., 2013). The latter data set was the monthly DOMINO ver. 2.0 collection 3, at a resolution of 0.125° × 0.125°, available from the Tropospheric Emission Monitoring Internet Service (TEMIS) website (http://www.temis.nl/airpollution/no2col/no2regioomimonth_col3.php; Boersma et al., 2011). The data at the nearest grid were used for both products. For the DOMINO algorithm, the results at eight adjacent grids were included (gray lines in Fig. 7) in addition to the nearest grid, to represent the spatial inhomogeneity of NO_2 over the range 0.375° × 0.375°.

The two algorithms subtract stratospheric NO_2 component as simulated by a chemical transport model (DOMINO ver 2.0) or determined directly from satellite data (NASA ver. 2.1) from the total and then determine TropoNO2VCD using tropospheric air mass factors. For both satellite data products, air mass factors were computed as average of clear and cloudy conditions weighted by the cloud radiation fraction, and therein the aerosols are implicitly taken into account similarly to clouds (Boersma et al., 2011; Bucsela et al., 2013). They both adopt the vertical profile shapes of NO_2 simulated by global chemical transport models at relatively coarse resolutions (TM4 at 2° × 3° for DOMINO and GMI at 2° × 2.5° for NASA) but with down to monthly time resolution. The uncertainty for individual retrievals of TropoNO2VCD was estimated to be 1.0×10^{15} molecules cm^{-2} + 25% (Boersma et al., 2011), and on the order of 10^{15} molecules cm^{-2} (Bucsela et al., 2013) for clear-sky conditions. Observational information content with respect to vertical profiles of NO_2 and the amount of aerosols is less than the case of MAX-DOAS observations; advantages of MAX-DOAS are that 1) observations of ΔSCDs of NO_2 at multiple axes are available, 2) simultaneous determination of aerosols is enabled using O_4 absorbance determined in the same axes, and 3) the determined aerosol quantities are explicitly taken into account in the NO_2 retrievals, although data at fixed locations with the instruments are only available.

3 Results and Discussion

We focus on NO_2 in this paper, so evaluation of our AOD results is included in the supplementary material. The NO_2 data obtained at Yokosuka and Hedo have been partly used for validation of TropoNO2VCD derived from OMI and other satellite sensors (Irie et al., 2009a, 2012), comparisons with ship-based observations (Takashima et al., 2012), and for analysis of transport from the Asian continent (Takashima et al., 2011). In this paper, independently of previous papers, we focus on features of temporal variations at multiple time scales (e.g., diurnal, weekly, and seasonal variations) of TropoNO2VCD. Comparisons with satellite-based TropoNO2VCD are also made wherever possible. Finally, we include comparisons with the simulation results from a global chemical transport model at Cape Hedo and Fukue.

3.1 Variations on seasonal or longer scales: comparisons with OMI

Figure 6 shows the full records of the TropoNO2VCDs for all the sites, including data during the whole daytime period, until December 2012. Table 1 summarizes the number of successful NO_2 retrievals for each site; in total, 80,927 data are included in the analysis in this paper. They are subsets of 180,654 data for which ΔSCDs of NO_2 and O_4 for all elevation angles were successfully determined and 90,644 data for which aerosol retrievals were successful, after careful data screening with respect to the instrumental conditions. The VCD levels were highest (at around 10^{16}–10^{17} molecules cm^{-2}) at Yokosuka, an urban site, and lowest (at around 3×10^{14} to 5×10^{15} molecules cm^{-2}) at Cape Hedo, a remote site; the VCD levels from other sites (Hefei, Gwangju, Zvenigorod, and Fukue, in descending order) were between these. Altogether, our TropoNO2VCD data ranged over more than two orders of magnitudes. The wide dynamic range and its full coverage were advantageous for the validation of satellite data, as shown later.

417 Figure 7 shows time series of monthly averaged MAX-DOAS observations (during
418 1300–1400 LT, except for 1500–1600 LT at Zvenigorod, matching satellite overpass timings)
419 and satellite observations of TropoNO2VCD from the OMI sensor. As mentioned in Section
420 2.4, two different products with different algorithms (NASA and DOMINO) were used.
421 At Cape Hedo and Fukue, where the local sources were negligible and thus the
422 observations were ideally representative over the grids described above (or over the footprint
423 size of the satellite observations, i.e., 24 × 13 km^2 or larger), the concentration levels and
424 variation patterns were in relatively good agreement (Fig. 7a and b). At the two sites, the
425 previous data product from NASA (ver. 1) always yielded significantly higher levels (Fig. 7a
426 and b). After revision of the data set, disagreements with the MAX-DOAS observations
427 disappeared and the agreement improved. For relatively low ranges of TropoNO2VCD (<~3 ×
428 10^{15} molecules cm^{-2}), precise subtraction of the stratospheric component of NO_2 is important
429 for satellite observations; this might have been the source of differences, although full
430 identification of the cause is beyond the scope of this paper.
431 The monthly variation pattern at Zvenigorod (Fig. 7f), in the middle range, i.e., ~10 × 10^{15}
432 molecules cm^{-2}, is very well reproduced by the satellite observations. The satellite data
433 capture the decreasing and increasing trends found using the MAX-DOAS observations from
434 April to October in 2011 and 2012, respectively.
435 In contrast, in polluted areas with TropoNO2VCD values normally exceeding 10 × 10^{15}
436 molecules cm^{-2}, for example, at Yokosuka and Gwangju (Fig. 7c and d), the MAX-DOAS
437 observations tended to be higher than both satellite-derived values. The spatial variability of
438 the NO_2 values over the nine grids for the DOMINO data set was relatively small and did not
439 extend to the average levels of the MAX-DOAS observations in winter at Yokosuka. This
440 may indicate that spatial inhomogeneity alone cannot explain the difference between the
441 MAX-DOAS and satellite observations, although the inhomogeneity at scales smaller than
442 0.125° could be responsible for the differences. It should be noted that the MAX-DOAS

observations are representative over a distance of about 2–10 km on the line of sight.

Figures 8a and b show summary scatterplots of the monthly averaged TropoNO2VCD values from observations by MAX-DOAS and those by OMI with two algorithms, DOMINO ver. 2.0 and NASA ver. 2.1. The correlations were very tight for both cases, with R^2 values exceeding 0.84, suggesting that the two satellite-derived products captured monthly variations quite well. However, the slopes were ~0.5 for both cases, suggesting that the satellite observations tended to give lower values than the MAX-DOAS observations did, and were strongly influenced by the data in the high range. The deviation from unity cannot be explained by the combined uncertainties in the satellite observations (~25%, Boersma et al., 2011) and MAX-DOAS.

When we limited the data to months where 1) more than 50% of the days of satellite observations were overlapped with MAX-DOAS observations and vice versa, and 2) coincident observations were made on 5 or more days, the R^2 value became even larger (R^2 = 0.88), but the slope remained at around 0.5. When the observation sites were grouped into two types, i.e., urban/suburban (Yokosuka, Gwangju, and Hefei) and rural/remote (Zvenigorod, Fukue, and Cape Hedo), the slopes were almost unchanged (0.54) for the urban/suburban case, whereas those for the rural/remote type increased to 0.78 and 0.63 with R^2 values of 0.74 and 0.65, with respect to DOMINO and NASA products, respectively (Figs 8c and d). This suggested the possibility that the observations at the three sites categorized as urban/suburban type did not represent the grids, and the spatial inhomogeneity could partly explain the larger departure of the slope value from unity.

This magnitude relationship was the opposite to those found in previous validation studies, which suggested the DOMINO products (ver. 1.02) had a high bias, i.e., 0–40% (Hains et al., 2010; Huijnen et al., 2010; Lamsal et al., 2010; Zhou et al., 2009), as summarized by Boersma et al. (2011). The revisions from DOMINO ver. 1.02 to the current version (ver. 2.0) were too small at the three urban/suburban sites (i.e., Yokosuka, Gwangju, and Hefei) to

explain the different results. However, recent studies suggested low biases, 26–38% and ~50%, in Beijing and in Delhi and its surroundings, respectively (Ma et al., 2013; Shaiganfar et al., 2011), in agreement with the magnitude relationship we found for the three urban/suburban sites.

Figure 9 shows the scatterplots between MAX-DOAS and OMI satellite observations at satellite pixel levels (n = 813, for six sites altogether) using more strict coincidence criteria (horizontal displacement <0.15°, time difference <15 min) and cloud screening (cloud fraction <10%). This also resulted in a similar underestimation of TropoNO2VCD for the satellite data; the slopes were 0.53 and 0.46, against DOMINO (ver. 2.0) and NASA (ver. 2.1), respectively. The slopes for the three cleaner sites were similar (0.55 and 0.42, respectively). This analysis indicated that a slope value lower than unity cannot be attributed to the poor overlap of the measurement days in each month or to the spatial inhomogeneity down to the scales of the footprint size of the satellite observations.

Another possibility would be that systematic underestimation by satellite observations arises from assumptions in the vertical profiles and aerosol treatment. Figure 10a shows that low OMI(NASA)/MAX-DOAS ratios (using a gridded data set for OMI) are associated with high AODs (as observed by MAX-DOAS); although the median ratio is near unity at low AODs (~0.1), it becomes lower (~0.7) with AODs as high as 1. In this study, only data with more than 1×10^{15} molecules cm^{-2} for both MAX-DOAS and satellite observations are used. This suggests the possibility that the satellite observations underestimate TropoNO2VCD when aerosols are densely present. This is less likely to be explained by overestimation by MAX-DOAS at high AODs, where larger observational information content regarding aerosols (multiple axis measurements of O_4) were used in the derivation of A_{box} and TropoNO2VCD. All of the data (n = 1834 from the six sites) were subdivided into two groups of equal size, based on AOD values (i.e., two groups with high and low AOD values) and a Welch's t-test was applied to test the statistical significance of the difference between the two

means. The results suggested that the OMI(NASA)/MAX-DOAS ratio was significantly lower for the group with higher AODs at the 95% confidence level. Similar tests for individual sites led to the same conclusion for Fukue, Zvenigorod, and Gwangju.

Figure 10b shows that the OMI(NASA)/MAX-DOAS ratio for TropoNO2VCD had a weak decreasing trend with the retrieved parameter v_1, the fraction of NO_2 present in the lowest 1 km. The median values decreased from around unity to 0.67 as v_1 increased from ~0.6 to 0.9. Welch's t-tests applied to two groups of data sorted by v_1 values suggested that the ratio was significantly lower for the group with higher v_1 values when using data from all six sites and when using data from Yokosuka and Hefei individually, at the 95% confidence level. This suggests that the underestimation occurs when NO_2 is mostly present near the surface. These analyses, in combination, imply that the lower values from the satellite could be partly caused by the assumptions made regarding the vertical profiles and aerosol treatment in the satellite data analysis. This may be important at clean sites, where the spatial inhomogeneity cannot be responsible for the difference. For both satellite data products, air mass factors were computed as average of clear and cloudy conditions weighted by the cloud radiation fraction, and therein the aerosols are implicitly taken into account similarly to clouds (Boersma et al., 2011; Bucsela et al., 2013). Considering that the variance of the ratio was only partly explained by AOD (Fig. 10a), one could argue that the effect of aerosols was almost successfully removed even in the current satellite data retrieval. However, a weak dependence of the ratio on AOD was still discernible, suggesting that the retrieval could be improved by an explicit treatment of the aerosols. Leitão et al. (2010) theoretically demonstrated that such underestimation by satellite observations could occur when the aerosol layer extends to relatively higher altitudes than NO_2. Recently, Shaiganfar et al. (2011) and Ma et al. (2013) implied that the shielding effect of NO_2 by aerosols could be the cause of low biases in OMI observations over India and China. Lin et al. (2013) suggested that concentration of aerosols at the top of the boundary layer increased retrieved NO_2 by 8%.

From the above analyses of correlations and dependences on AOD and v_1, we conclude that the values of the OMI satellite data for TropoNO2VCD were lower than those from the network MAX-DOAS observations, and were possibly affected by the presence of aerosols, the assumptions made regarding the vertical profile of NO_2, and how representative the site is (for the urban/suburban cases).

Figure 11 shows the averaged seasonal variations in the MAX-DOAS and satellite-based observations. MAX-DOAS data recorded during 1300–1400 LT (1500–1600 LT for Zvenigorod), matching satellite overpass timings, were used. Here, the right-axis scales for the OMI-derived quantities were adjusted by factors of 1.23, 1.54, 1.76, 1.77, 1.71, and 1.07 for Cape Hedo, Fukue, Yokosuka, Gwangju, Hefei, and Zvenigorod, respectively. At almost all sites except Zvenigorod, TropoNO2VCD had a clear summer minimum and winter maximum. This feature can be interpreted using a combination of 1) seasonal changes in NO_x emissions, 2) efficient partitioning to NO via faster photolysis rates of NO_2 in summer, and 3) efficient oxidation of NO_2 by OH in summer. Van der A et al. (2008) suggested, based on their analysis of GOME and SCIAMACHY (SCanning Imaging Absorption spectroMeter for Atmospheric CartograpHY) satellite data that the wintertime maximum indicates the dominance of NO_x sources from anthropogenic sectors (fossil fuel and biofuel combustion). Each of our observation sites had unique features in their seasonal patterns (Fig. 11), and the satellite data captured such detailed features quite well. For example, seasonal variations at Fukue Island and Hefei were relatively symmetric with respect to June/July. At Yokosuka and Gwangju, decreases in spring were slow, but increases in fall were relatively rapid. The wintertime peak occurred in December at Gwangju, whereas it appeared in January at Hefei. At Zvenigorod, low levels lasted for a short period during June–August, and the values in April and May, and in October, were larger. All these detailed features were quite well reproduced by the satellite observations.

Deviations of pixel-level OMI(NASA) TropoNO2VCD from monthly mean values

positively correlated with those for coinciding MAX-DOAS observations (Fig. 12, with R^2 values of 0.45) with a slope of 0.40, a similar value of those in Fig. 9. This suggested that the satellite observation successfully captured day-to-day variations in addition to the monthly variations, although the sensitivity was consistently small.

The observed features in the year-to-year variations were also well reproduced by the satellite observations (Fig. 7). For example, relatively high values in January 2011 at Cape Hedo, and those in December 2009 and January 2010 at Fukue were well captured.

3.2 Diurnal and weekly variations

Figure 13 shows the diurnal variations averaged for each month. Generally, daytime decreases were recorded, as a result of 1) stronger emissions in the early morning, 2) effective partitioning to NO in the daytime by NO_2 photolysis, and 3) stronger oxidation of NO_2 by OH, similar to the causes for the summer minima. At Cape Hedo, such a pattern of daytime decreases was clearly seen for all months (Fig. 13a). In contrast, at Yokosuka, Gwangju, and Hefei (Fig. 13c–e) in winter, daytime increases in TropoNO2VCD were observed. The periods with daytime increases were November–February at Yokosuka, November–December at Gwangju, and December–January at Hefei, slightly different from site to site. This feature was interpreted as 1) accumulation of pollutants overriding the loss rates and/or 2) importing of more polluted air masses in the afternoon period. Particularly at Yokosuka, located about 30 km south of the Tokyo metropolitan area, the wintertime northerly wind tended to carry more polluted air masses from northern areas near Tokyo to the south, resulting in higher NO_2 concentrations in the afternoon. Similar daytime increases in TropoNO2VCD duting winter were reported in Greenbelt, Maryland, USA (Wenig et al., 2008) and in/near Beijing, China (Ma et al., 2013; Hendrik et al., 2013). Figure 14a shows that the diurnal variation patterns for the partial column of NO_2 in the 0–1 km altitude range in four selected months, January, April, July, October at Yokosuka, are quite similar to those for NO_2 measured at a nearby

573 air-quality-monitoring site (Nagahama site, about 4 km to the northwest). The NO_2
574 monitoring was performed using a chemiluminescence instrument equipped with a
575 molybdenum converter, and thus was potentially influenced by other NO_z species; in the
576 urban locations near Tokyo, however, the influence was small (e.g., Kondo et al., 2008). In
577 this study, we only compared the diurnal patterns. In the afternoons in January, the patterns
578 were significantly different. The air mass on the line of sight of MAX-DOAS over Tokyo Bay
579 could have been more influenced by the transport of polluted air masses from the Tokyo
580 region or by ship emissions in the afternoon in winter.

581 Figure 15 shows the diurnal variations averaged separately for each day of the week.
582 Apparent holidays for each country were re-categorized as Sundays. Although almost no
583 weekend reductions were observed at remote locations (Cape Hedo and Fukue, Fig. 15a and
584 b), the TropoNO2VCD values were clearly lower on Sundays at Yokosuka and Gwangju,
585 because of the lower emissions from nearby sources, primarily as a result of less traffic (e.g.,
586 diesel trucks). At a similar suburban site, i.e., Hefei, however, this weekly cycle was not
587 observed (Fig. 15e). This different behavior suggests that the NO_x emission rate from the
588 major sector there does not follow a weekly cycle. It has been estimated from an Asian
589 emission inventory for INTEX-B for 2006 that 24%, 58%, and 61% of NO_x emission are from
590 the transportation sector for China, Korea, and Japan, respectively (Zhang et al., 2009). The
591 lower contribution from the transport sector for China probably causes this difference. The
592 negligible weekly variation in China was consistent with the results of an earlier study using
593 GOME data (Beirle et al., 2003). Similar results without weekend anomalies were found by
594 Ma et al. (2013) for MAX-DOAS observations in Beijing.

595 Figure 14b shows that the average diurnal profiles of the partial vertical columns of NO_2 in
596 the 0–1 km altitude range for weekdays, Saturdays, and Sundays at Yokosuka are in nearly
597 perfect agreement with those for NO_2 monitoring at the Nagahama site. These analyses of
598 diurnal and weekly behaviors of NO_2 help to refine the emission inventory of NO_x. For the

599 Kanto area, including Yokosuka and Tokyo, NO_x emissions on Sundays were estimated to be
600 lower by 45% (Kannari et al., 2007) for the year 2000, which is roughly in agreement with
601 our observations (37% reduction on Sundays for 0700–1600 LT). A more detailed comparison
602 between observed and modeled NO_2 at Yokosuka is planned, to refine the emission
603 inventories and to test the unique wintertime diurnal variation there.

604 Figure 16 compares the MAX-DOAS-derived reduction ratios for TropoNO2VCD at
605 weekends (for Saturdays and Sundays separately) with respect to weekdays, during
606 1300–1400 LT (1500–1600 LT for Zvenigorod), with those from OMI satellite observations
607 (using the NASA algorithm). The reduction ratios for Yokosuka, Gwangju, and Zvenigorod
608 for Sundays were 0.57, 0.89, and 0.71 for OMI, similar to 0.59, 0.76, and 0.85 for
609 MAX-DOAS. On Saturdays, the reduction ratios were commonly larger, and were almost
610 unity at Zvenigorod. The ratios for MAX-DOAS at Hefei were somewhat larger, but this
611 could be a result of the small number of data available for this specific hour.

612

613 **3.3 Comparison with model simulations**

614 The climatology based on the TropoNO2VCD values observed with MAX-DOAS at Cape
615 Hedo and Fukue, relatively remote locations, was compared with the simulation results
616 derived from a global chemical transport model, MIROC-ESM-CHEM (Watanabe et al.,
617 2012), based on CHASER (Sudo et al., 2002), to evaluate the model simulations. The model
618 included stratospheric/tropospheric chemistry and aerosol schemes, and had a spatial
619 resolution of 2.8° × 2.8° and 32 vertical layers. The wind field was assimilated using National
620 Centers for Environmental Prediction data. HadISST/ICE
621 (http://badc.nerc.ac.uk/view/badc.nerc.ac.uk__ATOM__dataent_hadisst) data were used for
622 the sea surface temperature. The simulations were made for 6 years (2007–2012) and the
623 average seasonal and diurnal variations were compared with the observations. The used
624 emission inventory was derived from Cofala et al. (2007), but the baseline year was updated

to 2005. The NO_x emissions and concentrations in east Asia could therefore be underestimated for the study period, because the emission rates have increased since 2005.

In Fig. 17, seasonal variations in TropoNO2VCD at different sites during 1300–1400 LT are compared. For Cape Hedo, the concentrations in all seasons except winter were quite well reproduced by the model simulations. To our knowledge, this is the first use of the climatology of TropoNO2VCD values in such a low range, as observed at remote islands, to evaluate global chemical transport model simulations. The seasonal variations, with summertime minima and wintertime maxima, were also well reproduced, although the model tended to underestimate wintertime values. Similar features were observed in the comparison with Fukue Island (Fig. 17b), where the wintertime underestimation was more significant than that for Cape Hedo. Because Fukue Island is located nearer to NO_x source regions in the Asian continent (including the Korean Peninsula), possible underestimation of NO_x emissions on the continent could explain the differences during the winter, when air masses generally originate from the Asian continent. In contrast, during summer, clean air masses reached the two sites from the open Pacific Ocean. Our results therefore suggested that the model simulation is valid in summer under such conditions, where the TropoNO2VCD values were as low as $0.6–1.5 \times 10^{15}$ molecules cm^{-2}.

Figure 18 compares the observed and modeled diurnal variations of TropoNO2VCD during four seasons. At Cape Hedo, the concentrations and detailed diurnal patterns, including daytime decreases and their rates in June–August (JJA) and September–November (SON), were almost perfectly reproduced by the model simulations. For Fukue, the rate of decrease at midday in JJA was also well captured by the model. This analysis again indicated that the NO_2 chemistry during the daytime was well simulated in the model, especially in summer.

3.4 Data availability

Numerical data files for the MADRAS network observations are available at

651 http://ebcrpa.jamstec.go.jp/maxdoashp. The files include TropoNO2VCD, AOD, vertical
652 profiles of NO_2, and extinction coefficients, with a 1-km resolution (up to 3 km) and a time
653 resolution of 30 min. The color index information is also included (see the supplementary
654 material for details).
655
656 **4 Summary**
657 Long-term network observations of TropoNO2VCD were conducted at seven sites, in Japan,
658 Korea, China, and Russia, covering remote to urban areas, from 2007, using standardized
659 MAX-DOAS instruments. A single algorithm was applied to the raw spectra obtained at the
660 sites to derive the ΔSCDs of NO_2 and O_4, and to estimate TropoNO2VCD optimally, using the
661 aerosol information derived from the O_4 observations. A large number (>80,000) of the
662 TropoNO2VCD values were used to test satellite observations of TropoNO2VCD from OMI
663 and model simulations, and to investigate the climatology of NO_2. The results were similar for
664 two satellite data products with different retrieval algorithms (DOMINO ver. 2.0 and NASA
665 ver. 2.1); the satellite observations had low biases, i.e., ~50%, whereas they were tightly
666 correlated with the MAX-DOAS observations and showed closely matching seasonalities.
667 Our analysis showed that the low biases could be attributed to the inhomogeneity of NO_2 on
668 the spatial scale of the data products from OMI observations, and incomplete accounting for
669 NO_2 present near the surface, possibly related to the shielding effect caused by the co-existing
670 aerosols, for the satellite observations. Future satellite observations with smaller footprint
671 sizes may help distinguishing the causes.
672 The average diurnal variations in TropoNO2VCD generally showed daytime decreases
673 during the summer but increases during the winter at urban/suburban sites. Weekend
674 reductions in NO_2 were clearly seen at Yokosuka and Gwangju, as a result of a reduction in
675 the amount of traffic, but did not occur at Hefei, China, where the major emitting sector was
676 probably different. The diurnal and weekly cyclic patterns at Yokosuka were in good

agreement with those derived from ground-based-monitoring data recorded near the site. A global chemical transport model, MIROC-ESM-CHEM, was validated for the first time with respect to background-level NO_2 column densities at Cape Hedo and Fukue during the summer, under the influence of marine air masses from the Pacific Ocean.

Acknowledgments

We thank Prede Co., Ltd. for technical assistance in developing instruments. Support from Y. Takeda and M. Kubo at the observatory is gratefully acknowledged. Drs. A. Takami and A. Shimizu (National Institute of Environmental Studies), T. Takamura (Chiba University), Y. Komazaki (Japan Agency for Marine and Earth Science and Technology) logistically supported our observations. We are grateful for free use of tropospheric NO_2 column data from the OMI sensor from www.temis.nl and from NASA. This work was supported by the Environmental Research and Technology Development Fund (S-7) of the Ministry of the Environment, Japan, by the Japan EOS Promotion Program (JEPP) and KAKENHI Grant numbers 25220101 and 26550022 of the Ministry of Education, Culture, Sports, Science, and Technology in Japan, by JSPS and RFBR (research project No. 12-05-92108_Jap_a and 11-05-01175-a) under the Japan-Russia Research Cooperative Program, and by the GEMS program of the Ministry of Environment, Korea and the Eco Innovation Program of KEITI (2012000160004).

References

Beirle, S., Platt, U., Wenig, M., and Wagner, T.: Weekly cycle of NO_2 by GOME measurements: a signature of anthropogenic sources, Atmos. Chem. Phys., 3, 2225-2232, 2003.

Boersma, K. F., Eskes, H. J., Veefkind, J. P., Brinksma, E. J., van der A, R. J., Sneep, M., van den Oord, G. H. J., Levelt, P. F., Stammes, P., Gleason, J. F., and Bucsela, E. J.: Near-real time retrieval of tropospheric NO_2 from OMI, Atmos. Chem. Phys., 7, 2103-2118, doi:10.5194/acp-7-2103-2007, 2007.

Boersma, K. F., Eskes, H. J., Dirksen, R. J., van der A, R. J., Veefkind, J. P., Stammes, P., Huijnen, V., Kleipool, Q. L., Sneep, M., Claas, J., Leitão, J., Richter, A., Zhou, Y., and Brunner, D.: An improved tropospheric NO2 column retrieval algorithm for the Ozone Monitoring Instrument, Atmos. Meas. Tech., 4, 1905-1928, doi:10.5194/amt-4-1905-2011, 2011.

Bogumil, K., Orphal, J., Homann, T., Voigt, S., Spietz, P., Fleischmann, O. C., Vogel, A., Hartmann, M., Bovensmann, H., Frerik, J., and Burrows, J. P.: Measurements of molecular absorption spectra with the SCIAMACHY Pre-Flight Model: Instrument characterization and reference spectra for atmospheric remote sensing in the 230–2380 nm region, J. Photochem. Photobiol. A., 157, 167–184, 2003.

Brinksma, E. J., Pinardi, G., Volten, H., Braak, R., Richter, A., Schönhardt, A., van Roozendael, M., Fayt, C., Hermans, C., Dirksen, R. J., Vlemmix, T., Berkhout, A. J. C., Swart, D. P. J., Oetjen, H., Wittrock, F., Wagner, T., Ibrahim, O. W., de Leeuw, G., Moerman, M., Curier, R. L., Celarier, E. A., Cede, A., Knap, W. H., Veefkind, J. P., Eskes, H. J., Allaart, M., Rothe, R., Piters, A. J. M., and Levelt, P. F.: The 2005 and 2006 DANDELIONS NO_2 and aerosol intercomparison campaigns, J. Geophys. Res., 113, D16S46, doi:10.1029/2007JD008808, 2008.

Bucsela, E. J., Perring, A. E., Cohen, R. C., Boesma, K. F., Celarier, E. A., Gleason, J. F., Wenig, M. O., Bertram, T. J., Wooklridge, P. J., Dirksen, R., and Veefkind, J. P.: Comparison of tropospheric NO_2 from in situ aircraft measurements with near-real-time and standard product data from OMI, J. Geophys. Res., 113, D16S31, doi:10.1029/2007JD008838, 2008.

Bucsela, E. J., Krotkov, N. A., Celarier, E. A., Lamsal, L. N., Swartz, W. H., Bhartia, P. K., Boersma, K. F., Veefkind, J. P., Gleason, J. F., and Pickering, K. E.: A new stratospheric and tropospheric NO_2 retrieval algorithm for nadir-viewing satellite instruments: applications to OMI, Atmos. Meas. Tech., 6, 2607-2626, doi:10.5194/amt-6-2607-2013, 2013.

Burrows, J, P., Weber, M., Buchwitz, M., Rozanov, V., Ladstätter-Weißenmayer, A., Richter, A., DeBeek, R., Hoogen, R., Bramstedt, K., Eichmann, K-U., Eisinger, M., and Perner, D.: Global ozone monitoring experiment (GOME): Mission concept and first scientific results, J. Atmos. Sci., 56, 171-175, 1999.

Celarier, E. A., Brinksma, E. J., Gleason, J. F., Veefkind, J. P., Cede, A., Herman, J. R., Ionov, D., Goutail, F., Pommereau, J. –P., Lambert, J. –C., van Roozendael, M., Pinardi, G., Wittrock, F., Schönhardt, A., Richter, A., Ibrahim, O. W., Wagner, T., Bojkov, B., Mount, G., Spinei, E., Chen, C. M., Pongetti, T. J., Sander, S. P., Bucsela, E. J., Wenig, M. O., Swart, D. P. J., Volten, H., Kroon, M., and Levelt, P. F.: Validation of Ozone Monitoring Instrument nitrogen dioxide columns, J. Geophys. Res., 113, D15S15, doi:10.1029/2007JD008908, 2008.

Chen, D., Zhou, B., Beirle, S., Chen, L. M., and Wagner, T.: Tropospheric NO_2 column

densities deduced from zenith-sky DOAS measurements in Shanghai, China, and their application to satellite validation, Atmos. Chem. Phys., 9, 3641-3662, doi:10.5194/acp-9-3641-2009, 2009.

Clémer, K., Van Roozendael, M., Fayt, C., Hendrick, F., Hermans, C., Pinardi, G., Spurr, R., Wang, P., and De Mazière, M.: Multiple wavelength retrieval of tropospheric aerosol optical properties from MAXDOAS measurements in Beijing, Atmos. Meas. Tech., 3, 863-878, 2010.

Cofala, J., Amann, M., Klimont, Z., Kupiainen, K., and Högund-Isaksson, L: Scenarios of global anthropogenic emissions of air pollutants and methane until 2030, Atmos. Environ., 41, 8486-8499, 2007.

Duce, R. A., LaRoche, J., Altieri, K., Arrigo, K. R., Baker, A. R., Capone, D. G., Cornell, S., Dentener, F., Galloway, J., Ganeshram, R. S., Geider, R. J., Jickells, T., Kuypers, M. M., Langlois, R., Liss, P. S., Liu, S. M., Middelburg, J. J., Moore, C. M., Nickovic, S., Oschlies, A., Pedersen, T., Prospero, J., Schlitzer, R., Seitzinger, S., Sorensen, L. L., Uematsu, M., Ulloa, O., Voss, M., Ward, B., and Zamora, L.: Impacts of Atmospheric Anthropogenic Nitrogen on the Open Ocean, Science, 320(5878), 893–897, 2008.

Fayt, C. and Van Roozendael, M.: QDOAS Software User Manual Version 2.00, http://uv-vis.aeronomie.be/software/QDOAS/ (last access April 2012), 2012.

Galle, B., Johansson, M., Rivera, C., Zhang, Y., Kihlman, M., Kern, C., Lehmann, T., Platt, U., Arellano, S., and Hidalgo, S.: Network for Observation of Volcanic and Atmospheric Change (NOVAC)—A global network for volcanic gas monitoring: Network layout and instrument description, J. Geophys. Res., 115, D05304, doi:10.1029/2009JD011823, 2010.

Hains, J. C., Boersma, K. F., Kroon, M., Dirksen, R. J., Cohen, R. C., Perring, A. E., Bucsela, E., Volten, H., Swart, D. P. J., Richter, A., Wittrock, F., Schoenhardt, A., Wagner, T., Ibrahim, O. W., van Roozendael, M., Pinardi, G., Gleason, J. F., Veefkind, J. P., and Levelt, P.: Testing and improving OMI DOMINO tropospheric NO_2 using observations from the DANDELIONS and INTEX-B validation campaigns, J. Geophys. Res., 115, D05301, doi:10.1029/2009JD012399, 2010.

Hendrick, F., Müller, J.-F., Clémer, K., De Mazière, M., Fayt, C., Hermans, C., Stavrakou, T., Vlemmix, T., Wang, P., and Van Roozendael, M.: Four years of ground-based MAX-DOAS observations of HONO and NO_2 in the Beijing area, Atmos. Chem. Phys. Discuss., 13, 10621-10660, doi:10.5194/acpd-13-10621-2013, 2013.

Heue, K.-P., Richter, A., Bruns, M., Burrows, J. P., v. Friedeburg, C., Platt, U., Pundt, I., Wang, P., and Wagner, T.: Validation of SCIAMACHY tropospheric NO_2-columns with AMAXDOAS measurements, Atmos. Chem. Phys., 5, 1039-1051, doi:10.5194/acp-5-1039-2005, 2005.

Holben, B.N., Tanre, D., Smirnov, A., Eck, T. F., Slutsker, I., Abuhassan, N., Newcomb, W.W., Schafer, J., Chatenet, B., Lavenue, F., Kaufman, Y. J., Vande Castle, J., Setzer, A., Markham, B., Clark, D., Frouin, R., Halthore, R., Karnieli, A., O'Neill, N. T., Pietras, C.,

Pinker, R. T., Voss, K., and Zibordi, G.: An emerging ground-based aerosol climatology: Aerosol Optical Depth from AERONET, J. Geophys. Res., 106, 12 067-12 097, 2001.

Hönninger, G., von Friedeburg, C., and Platt, U.: Multi axis differential optical absorption spectroscopy (MAX-DOAS), Atmos. Chem. Phys., 4, 231-254, doi:10.5194/acp-4-231-2004, 2004.

Huijnen, V., Eskes, H. J., Poupkou, A., Elbern, H., Boersma, K. F., Foret, G., Sofiev, M., Valdebenito, A., Flemming, J., Stein, O., Gross, A., Robertson, L., D'Isidoro, M., Kioutsioukis, I., Friese, E., Amstrup, B., Bergstrom, R., Strunk, A., Vira, J., Zyryanov, D., Maurizi, A., Melas, D., Peuch, V.-H., and Zerefos, C.: Comparison of OMI NO2 tropospheric columns with an ensemble of global and European regional air quality models, Atmos. Chem.Phys., 10, 3273–3296, doi:10.5194/acp-10-3273-2010, 2010.

Irie, H., Kanaya, Y., Akimoto, H., Tanimoto, H.. Wang, Z., Gleason, J. F., and Bucsela, E. J.: Validation of OMI tropospheric NO2 column data using MAX-DOAS measurements deep inside the North China Plain in June 2006, Atmos. Chem. Phys., 8, 6577-6586, 2008a.

Irie, H., Kanaya, Y., Akimoto, H.. Iwabuchi, H., Shimizu, A., and Aoki, K.: First retrieval of tropospheric aerosol profiles using MAX-DOAS and comparison with lidar and sky radiometer measurements, Atmos. Chem. Phys., 8, 341-350, 2008b.

Irie, H., Kanaya, Y., Takashima, H., Gleason, J. F., and Wang, Z.: Characterization of OMI tropospheric NO_2 measurements in East Asia based on a robust validation comparison, SOLA, 5, 117-120, 2009a.

Irie, H., Kanaya, Y., Akimoto, H., Iwabuchi, H., Shimizu, A., and Aoki, K.: Dual-wavelength aerosol vertical profile measurements by MAX-DOAS at Tsukuba, Japan, Atmos. Chem. Phys., 9, 2741-2749, 2009b.

Irie, H., Takashima, H., Kanaya, Y., Boersma, K. F., Gast, L., Wittrock, F., Brunner, D., Zhou, Y., and Van Roozendael, M.: Eight-component retrievals from ground-based MAX-DOAS observations, Atmos. Meas. Tech., 4, 1027-1044, doi:10.5194/amt-4-1027-2011, 2011.

Irie, H., Boersma, K. F., Kanaya, Y., Takashima, H., Pan, X., and Wang, Z. F.: Quantitative bias estimates for tropospheric NO_2 columns retrieved from SCIAMACHY, OMI, and GOME-2 using a common standard, Atmos. Meas. Tech., 5, 2403-2411, doi:10.5194/amt-5-2403-2012, 2012.

Iwabuchi, H.: Efficient Monte Carlo methods for radiative transfer modeling, J. Atmos. Sci., 63, 9, 2324–2339, 2006.

Kanaya, Y., Sadanaga, Y., Nakamura, K., and Akimoto, H.: Behavior of OH and HO_2 radicals during the Observations at a Remote Island of Okinawa (ORION99) field campaign: 1. Observation using a laser-induced fluorescence instrument, J. Geophys. Res., 106(D20), 24197–24208, doi:10.1029/2000JD000178, 2001.

Kannari, A., Tonooka, Y., Baba, T., Murano, K.: Development of multiple-species 1 km × 1 k m resolution hourly basis emissions inventory for Japan, Atmos. Environ., 41, 3428-3439, 2007.

822 Kondo, Y., Morino, Y., Fukuda, M., Kanaya, Y., Miyazaki, Y., Takegawa, N., Tanimoto, H.,
823 McKenzie, R., Johnston, P., Blake, D. R., Murayama, T., and Koike, M.: Formation and
824 transport of oxidized reactive nitrogen, ozone, and secondary organic aerosol in Tokyo, J.
825 Geophys. Res., 113, D21310, doi:10.1029/2008JD010134, 2008.
826 Lamsal, L. N., Martin, R. V.. van Donkelaar, A., Celarier, E. A., Bucsela, E. J., Boersma, K.
827 F., Dirksen, R., Luo, C., and Wang, Y.: Indirect validation of tropospheric nitrogen dioxide
828 retrieved from the OMI satellite instrument: Insight into the seasonal variation of nitrogen
829 oxides at northern midlatitudes, J. Geophys. Res., 115, D05302,
830 doi:10.1029/2009JD013351, 2010.
831 Leitão, J., Richter, A., Vrekoussis, M., Kokhanovsky, A., Zhang, Q. J., Beekmann, M., and
832 Burrows, J. P.: On the improvement of NO_2 satellite retrievals – aerosol impact on the
833 airmass factors, Atmos. Meas. Tech., 3, 475-493, doi:10.5194/amt-3-475-2010, 2010.
834 Lin, J-T., Martin, R. V., Boersma, K. F., Sneep, M., Stammes, P., Spurr, R., Wang, P., Van
835 Roozendael, M., Clémer, K., and Irie, H.: Retrieving tropospheric nitrogen dioxide over
836 China from the Ozone Monitoring Instrument: Effects of aerosols, surface reflectance
837 anisotropy and vertical profile of nitrogen dioxide, Atmos. Chem. Phys. Discuss.,
838 21203-21257, 2013.
839 Ma, J. Z., Beirle, S., Jin, J. L., Shaiganfar, R., Yan, P., and Wagner, T.: Tropospheric NO_2
840 vertical column densities over Beijing: results of the first three years of ground-based
841 MAX-DOAS measurements (2008–2011) and satellite validation, Atmos. Chem. Phys., 13,
842 1547-1567, doi:10.5194/acp-13-1547-2013, 2013.
843 Martin, R. V., Sioris, C. E., Chance, K., Ryerson, T. B., Bertram, T. H., Wooldridge, P. J.,
844 Cohen, R. C., Neuman, J. A., Swanson, A., and Flocke, F. M.: Evaluation of space-based
845 constraints on global nitrogen oxide emissions with regional aircraft measurements over
846 and downwind of eastern North America, J. Geophys. Res., 111, D15308,
847 doi:10.1029/2005JD006680, 2006.
848 Peters, E., Wittrock, F., Großmann, K., Frieß, U., Richter, A., and Burrows, J. P.:
849 Formaldehyde and nitrogen dioxide over the remote western Pacific Ocean: SCIAMACHY
850 and GOME-2 validation using ship-based MAX-DOAS observations, Atmos. Chem. Phys.,
851 12, 11179-11197, doi:10.5194/acp-12-11179-2012, 2012.
852 Piters, A. J. M., Boersma, K. F., Kroon, M., Hains, J.C., Van Roozendael, M., Wittrock, F.,
853 Abuhassan, N., Adams, C., Akrami, M., Allaart, M. A. F., Apituley,A., Beirle, S., Bergwerff,
854 J. B., Berkhout, A. J. C., Brunner, D., Cede, A., Chong, J., Clémer, K., Fayt, C., Frieß, U.,
855 Gast, L. F. L., Gil-Ojeda, M., Goutail, F., Graves, R., Griesfeller, A., Großmann, K.,
856 Hemerijckx, G., Hendrick, F., Henzing, B., Herman, J., Hermans, C., Hoexum, M., van der
857 Hoff, G. R., Irie, H., Johnston, P. V., Kanaya, Y., Kim, Y. J., Klein Baltink, H., Kreher, K.,
858 de Leeuw, G., Leigh, R., Merlaud, A., Moerman, M. M., Monks, P. S., Mount, G. H.,
859 Navarro-Comas, M., Oetjen, H., Pazmino, A., Perez-Camacho, M., Peters, E., du Piesanie,
860 A., Pinardi, G., Puentedura, O., Richter, A., Roscoe, H. K., Schönhardt, A., Schwarzenbach,

B., Shaiganfar, R., Sluis, W., Spinei, E., Stolk, A. P., Strong, K., Swart, D. P. J., Takashima, H., Vlemmix, T., Vrekoussis, M., Wagner, T., Whyte, C., Wilson, K. M., Yela, M., Yilmaz, S., Zieger, P., and Zhou, Y.: The Cabauw Intercomparison campaign for Nitrogen Dioxide measuring Instruments (CINDI): design, execution, and early results, Atmos. Meas. Tech., 5, 457-485, doi:10.5194/amt-5-457-2012, 2012.

Platt, U., Differential optical absorption spectroscopy (DOAS), Chem. Anal. Series, 127, 27-83, 1994.

Richter, A., Burrows, J. P., Nuss, H., Granier, C., and Niemeier, U.: Increase in tropospheric nitrogen dioxide over China observed from space, Nature, 437, 129–132, 2005.

Rodgers, C. D.: Inverse methods for atmospheric sounding: Theory and practice, Ser. Atmos. Oceanic Planet. Phys., 2, edited by F. W. Taylor, World Sci., Hackensack, N. J., 2000.

Roscoe, H. K., Van Roozendael, M., Fayt, C., du Piesanie, A., Abuhassan, N., Adams, C., Akrami, M., Cede, A., Chong, J., Clémer, K., Friess, U., Gil Ojeda, M., Goutail, F., Graves, R., Griesfeller, A., Grossmann, K., Hemerijckx, G., Hendrick, F., Herman, J., Hermans, C., Irie, H., Johnston, P. V., Kanaya, Y., Kreher, K., Leigh, R., Merlaud, A., Mount, G. H., Navarro, M., Oetjen, H., Pazmino, A., Perez-Camacho, M., Peters, E., Pinardi, G., Puentedura, O., Richter, A., Schönhardt, A., Shaiganfar, R., Spinei, E., Strong, K., Takashima, H., Vlemmix, T., Vrekoussis, M., Wagner, T., Wittrock, F., Yela, M., Yilmaz, S., Boersma, F., Hains, J., Kroon, M., Piters, A., and Kim, Y. J.: Intercomparison of slant column measurements of NO_2 and O_4 by MAX-DOAS and zenith-sky UV and visible spectrometers, Atmos. Meas. Tech., 3, 1629-1646, doi:10.5194/amt-3-1629-2010, 2010.

Rothman, L. S., Barbe, A., Chris Benner, D., and Hitran-Team.: The HITRAN Molecular Spectroscopic Database: Edition of 2000 including updates through 2001, J. Quant. Spectrosc. Radiat. Transfer, 82, 5–44, 2003.

Shaiganfar, R., Beirle, S., Sharma, M., Chauhan, A., Singh, R. P., and Wagner, T.: Estimation of NOx emissions from Delhi using Car MAX-DOAS observations and comparison with OMI satellite data, Atmos. Chem. Phys., 11, 10871-10887, doi:10.5194/acp-11-10871-2011, 2011.

Sinreich, R., Frieß, U., Wagner, T., and Platt, U.: Multi axis differential optical absorption spectroscopy (MAX-DOAS) of gas and aerosol distributions, Faraday Discussions, 130, 153-164, doi: 10.1039/b419274p, 2005.

Sudo, K., Takahashi, M., Kurokawa, J., and Akimoto, H.: CHASER: A global chemical model of the troposphere 1. Model description, J. Geophys. Res., 107 (D17), 4339, doi:10.1029/2001JD001113, 2002.

Takami, A., Miyoshi, T., Shimono, A., Kaneyasu, N., Kato, S., Kajii, Y., and Hatakeyama, S.: Transport of anthropogenic aerosols from Asia and subsequent chemical transformation, J. Geophys. Res., 112, D22S31, doi:10.1029/2006JD008120, 2007.

Takashima, H., Irie, H., Kanaya, Y., Shimizu, A., Aoki, K., and Akimotom H.: Atmospheric aerosol variations at Okinawa Island in Japan observed by MAX-DOAS using a new

900 cloud-screening method, J. Geophys. Res., 114, D18213, doi:10.1029/2009JD011939,
901 2009.
902 Takashima, H., Irie, H., Kanaya, Y., and Akimoto, H.: Enhanced NO_2 at Okinawa Island,
903 Japan caused by rapid air mass transport from China as observed by MAX-DOAS, Atmos.
904 Environ., 45(15), 2593-2597, 2011.
905 Takashima, H., Irie, H., Kanaya, Y., and Syamsudin, F.: NO_2 observations over the western
906 Pacific and Indian Ocean by MAX-DOAS on Kaiyo, a Japanese research vessel, Atmos.
907 Meas. Tech. 5, 2351-2360, doi: 10.5194/amt-5-2351-2012, 2012.
908 Theys, N., Van Roozendael, M., Hendrick, F., Fayt, C., Hermans, C., Baray, J.-L., Goutail, F.,
909 Pommereau, J.-P., and e Mazière, M. D: Retrieval of stratospheric and tropospheric BrO
910 columns from Multi-Axis DOAS measurements at Reunion Island (21°S, 56°E), Atmos.
911 Chem. Phys., 7, 4733-4749, 2007.
912 Valks, P., Pinardi, G., Richter, A., Lambert, J.-C., Hao, N., Loyola, D., Van Roozendael, M.,
913 and Emmadi, S.: Operational total and tropospheric NO2 column retrieval for GOME-2,
914 Atmos. Meas. Tech., 4, 1491-1514, doi:10.5194/amt-4-1491-2011, 2011.
915 Vandaele, A. C., Hermans, C., Simon, P. C., Van Roozendael, M., Guilmot, J. M., Carleer, M.,
916 and Colin, R.: Fourier transform measurement of NO_2 absorption cross-section in the
917 visible range at room temperature, J. Atmos. Chem., 25, 289–305, 1996.
918 van der A, R. J., Eskes, H. J., Boersma, K. F., van Noije, T. P. C., Van Roozendael, M., De
919 Smedt, I., Peters, D. H. M. U., and Meijer, E. W.: Trends, seasonal variability and
920 dominant NOx source derived from a ten year record of NO_2 measured from space, J.
921 Geophys. Res., 113, D04302, doi:10.1029/2007JD009021, 2008.
922 Wagner, T., Burrows, J. P., Deutschmann, T., Dix, B., von Friedeburg, C., Frieß, U.,
923 Hendrick, F., Heue, K.-P., Irie, H., Iwabuchi, H., Kanaya, Y., Keller, J., McLinden, C. A.,
924 Oetjen, H., Palazzi, E., Petritoli, A., Platt, U., Postylyakov, O., Pukite, J., Richter, A., van
925 Roozendael, M., Rozanov, A., Rozanov, V., Sinreich, R., Sanghavi, S., and Wittrock, F.:
926 Comparison of box-air-mass-factors and radiances for Multiple-Axis Differential Optical
927 Absorption Spectroscopy (MAX-DOAS) geometries calculated from different UV/visible
928 radiative transfer models, Atmos. Chem. Phys., 7, 1809-1833,
929 doi:10.5194/acp-7-1809-2007, 2007.
930 Watanabe, S., Takemura, T., Sudo, K., Yokohata, T., and Kawase, H.: Anthropogenic
931 changes in the surface all-sky UV-B radiation through 1850–2005 simulated by an Earth
932 system model, Atmos. Chem. Phys., 12, 5249-5257, doi:10.5194/acp-12-5249-2012, 2012.
933 Wenig, M. O., Cede, A. M., Bucsela, E. J., Celarier, E. A., Boersma, K. F., Veefkind, J. P.,
934 Brinksma, E. J., Gleason, J. F., and Herman, J. R.: Validation of OMI tropospheric NO_2
935 column densities using direct-Sun mode Brewer measurements at NASA Goddard Space
936 Flight Center, J. Geophys. Res., 113, D16S45, doi:10.1029/2007JD008988, 2008.
937 Wittrock, F., Oetjen, H., Richter, A., Fietkau, S., Medeke, T., Rozanov, A., and Burrows, J. P.:
938 MAX-DOAS measurements of atmospheric trace gases in Ny-Ålesund - Radiative transfer

939 studies and their application, Atmos. Chem. Phys., 4, 955-966, 2004
940 Yurganov, L., McMillan, W., Grechko, E., and Dzhola, A., Analysis of global and regional CO
941 burdens measured from space between 2000 and 2009 and validated by ground-based solar
942 tracking spectrometers, Atmos. Chem. Phys., 10, 3479–3494, 2010.
943 Zhang, Q., Streets, D. G., Carmichael, G. R., He, K. B., Huo, H., Kannari, A., Klimont, Z.,
944 Park, I. S., Reddy, S., Fu, J. S., Chen, D., Duan, L., Lei, Y., Wang, L. T., and Yao, Z. L.:
945 Asian emissions in 2006 for the NASA INTEX-B mission, Atmos. Chem. Phys., 9,
946 5131-5153, doi:10.5194/acp-9-5131-2009, 2009.
947 Zhou, Y., Brunner, D., Boersma, K. F., Dirksen, R., and Wang, P.: An improved tropospheric
948 NO_2 retrieval for OMI observations in the vicinity of mountainous terrain, Atmos. Meas.
949 Tech., 2, 401–416, doi:10.5194/amt-2-401-2009, 2009.

Table 1. List of locations for MAX-DOAS observations.

Location	Type	Latitude (°N)	Longitude (°E)	Surface Elevation (m)	Instrument Elevation (m)	Azimuth angle (°, from North, clockwise)	N (NO_2 retrievals)	Instruments and used periods
Yokosuka	Urban	35.32	139.65	0	10	+37	26,554	#1 (Type A), Apr 2007–Dec 2012
Cape Hedo	Remote	26.87	128.25	0	68	−14	18,367	#1 (Type A), Mar 2007–Dec 2012
Gwangju	Suburban	35.23	126.84	30	43	+44	11,349	#1 (Type C), Feb 2008–Jun 2009 #2 (Type C), Nov 2009–Aug 2010 #3 (Type B), May 2011–Dec 2012
Hefei	Suburban	31.91	117.16	30	51	+22	5,324	#1 (Type C), Mar 2008–Oct 2009 #2 (Type C), Nov 2009–Dec 2012
Zvenigorod	Rural	55.70	36.78	186	208	−32	8,948	#1 (Type C), Oct 2008–Dec 2012
Tomsk	Suburban	56.48	85.05	160	188	0	-	#1 (Type C), Jan 2009–Dec 2012
Fukue	Remote	32.75	128.68	80	83	+30	10,385	#1 (Type B), Mar 2009–Apr 2009 #2 (Type C), Apr 2009–Mar 2012 #3 (Type B), Mar 2012–Dec 2012
TOTAL							**80,927**	

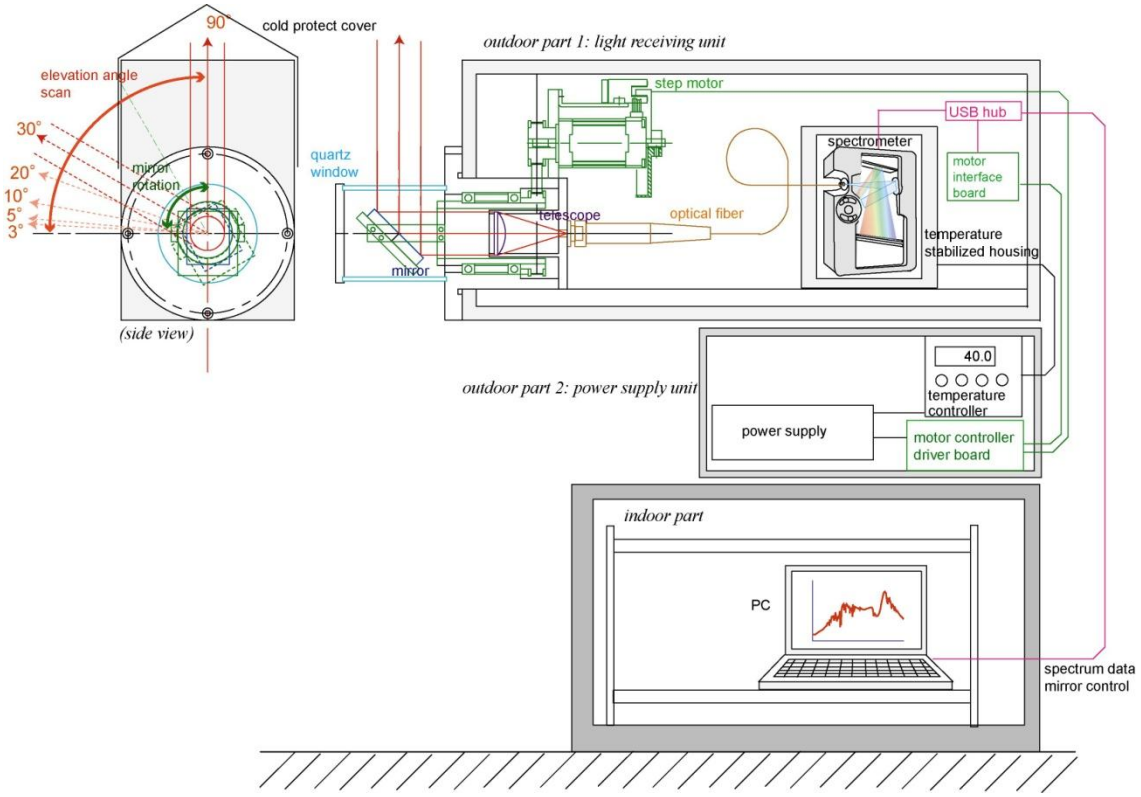

958

959 **Fig. 1.** Schematic diagram of MAX-DOAS instrument used at Zvenigorod.

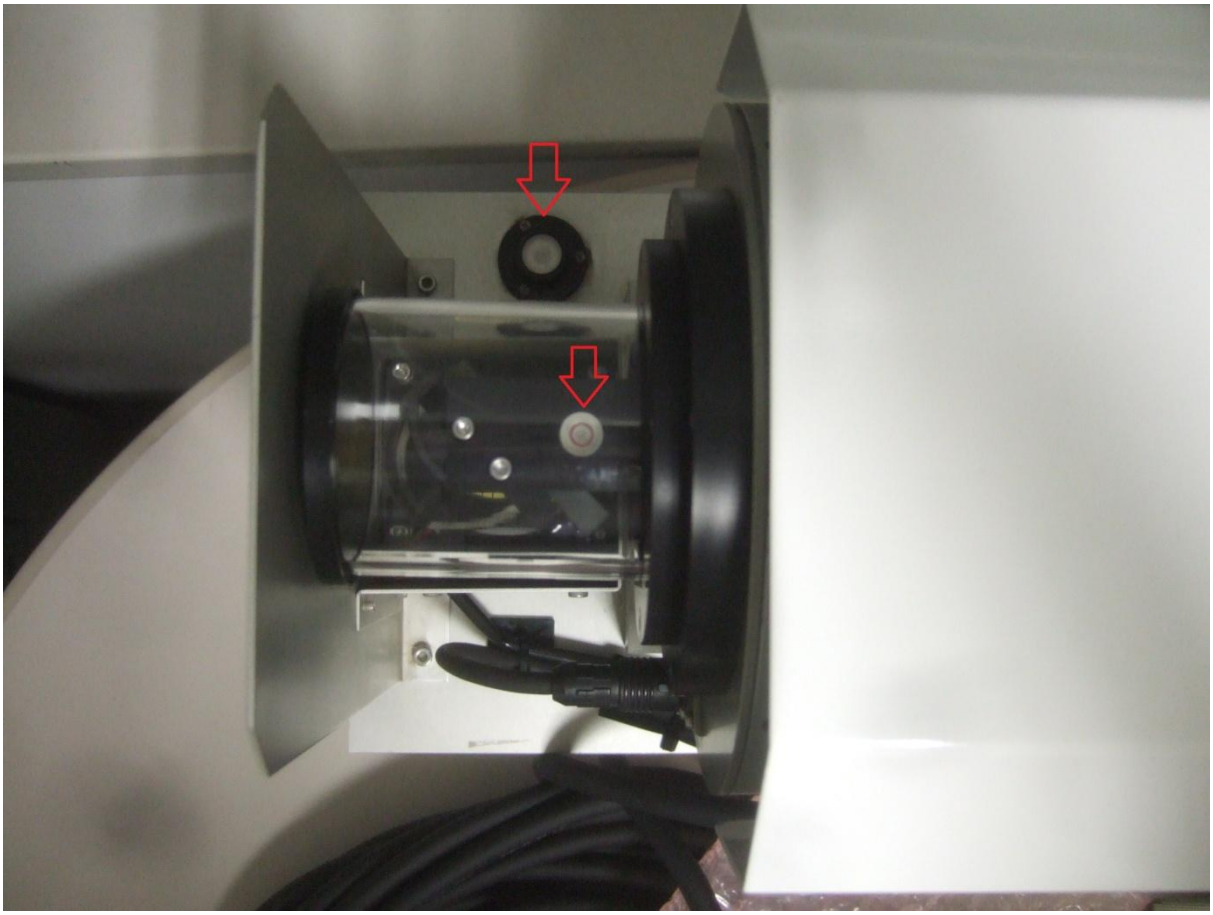

Fig. 2. Two horizontal levels embedded in the base plate (upper arrow) and in a plate holding the reflecting mirror (lower arrow) were used to adjust the zero angle of the reflecting mirror.

965

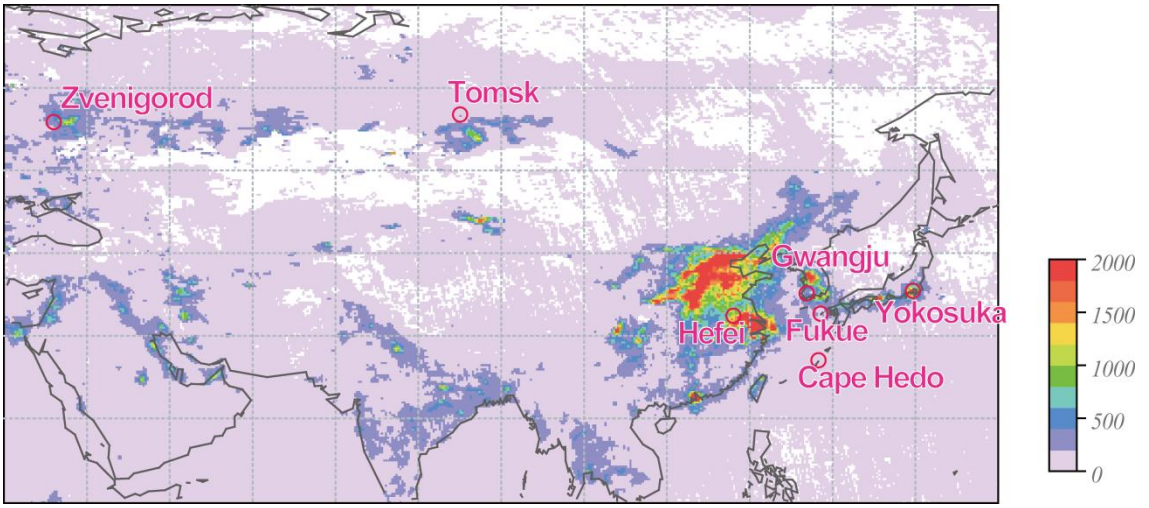

966 **Fig. 3.** Locations of our MAX-DOAS observations. The background contour is based on the

967 TropoNO_2VCD (10^{13} molecules cm^{-2}) observed by OMI (DOMINO ver. 2.0).

968

969

970 **Fig. 4.** Light-receiving parts of MAX-DOAS instruments located at the seven sites.

971

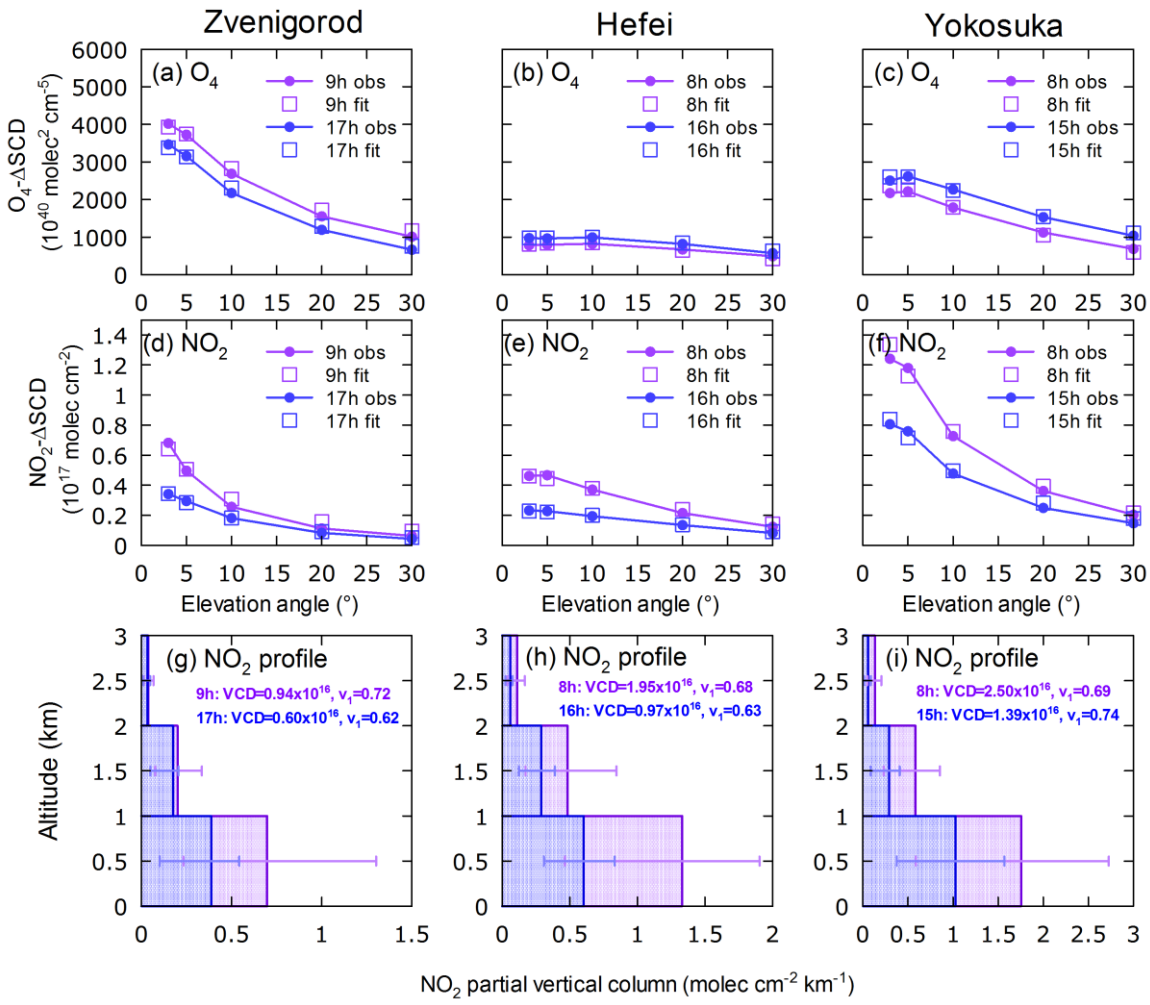

Fig. 5. (a)–(f) Observed and fitted O_4 ΔSCDs and NO_2 ΔSCDs, and (g)–(i) optimally estimated NO_2 vertical profiles averaged over each 1-h period in the morning and afternoon at Zvenigorod, Hefei, and Yokosuka sites, respectively. For (g)–(i), error bars represent 1σ range of individual profiles included in the hours.

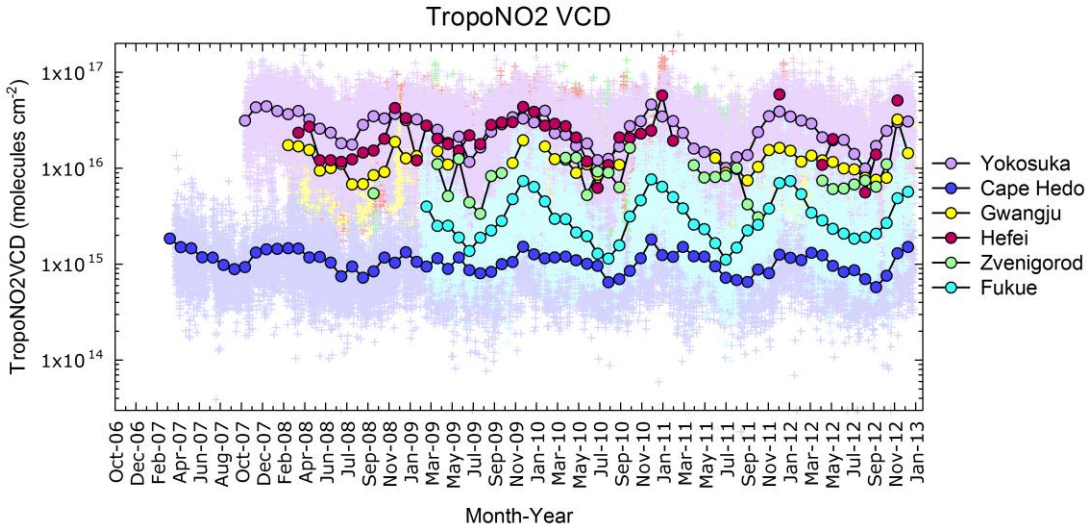

977

978

979 **Fig. 6.** Time series of all individual observations of TropoNO2VCD (plus signs, 30-min time

980 resolution) and their monthly averages (circles).

981

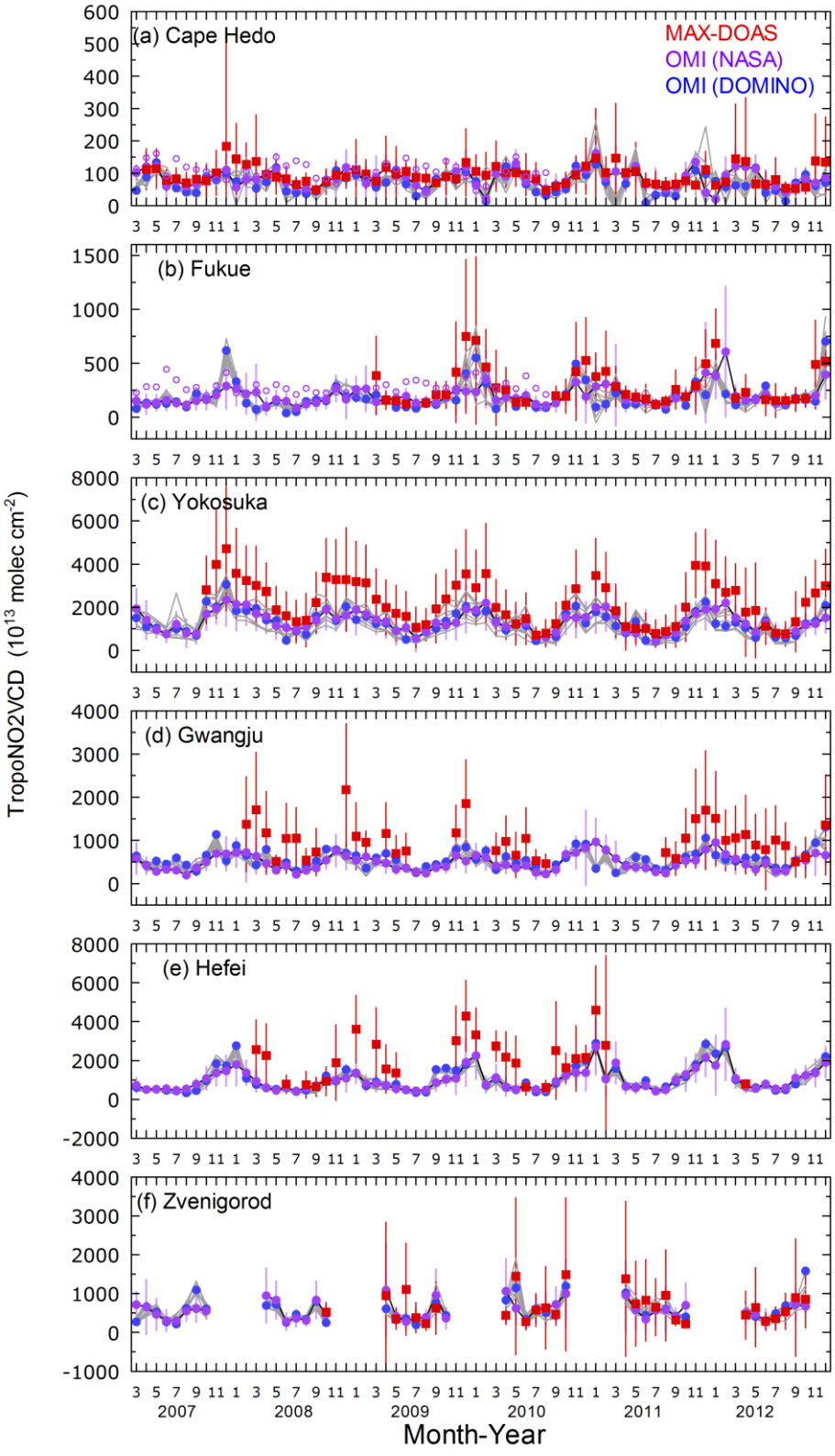

Fig. 7. Time series of monthly averages of MAX-DOAS (red) and satellite observations of TropoNO2VCD. The satellite observations are derived using NASA (ver. 2.1, purple) and DOMINO (ver. 2.0, blue) algorithms. Open purple circles in (a) and (b) represent data from

986 older products (NASA ver. 1). Error bars of MAX-DOAS represent 1σ ranges of included
987 data. Error bars of OMI with NASA ver. 2.1 algorithm were calculated from 1σ ranges of
988 daily data included in the month. Gray lines represent OMI data using DOMINO ver. 2.0
989 algorithm at the eight grids (0.125° × 0.125°) adjacent to the grid nearest the site (blue
990 circles).
991

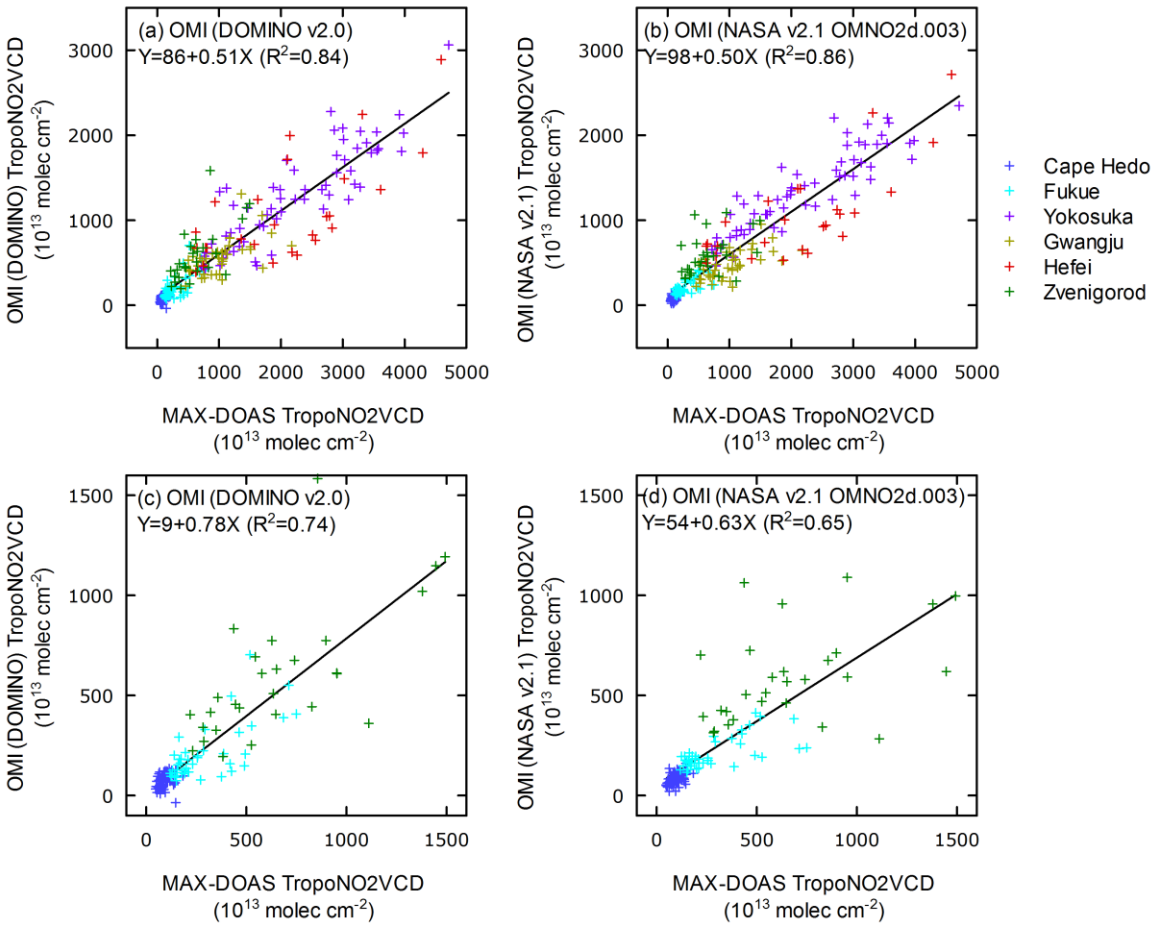

992

993 **Fig. 8.** Scatterplots between monthly averages of TropoNO2VCD derived from OMI and
994 MAX-DOAS for (a) and (b) all sites, and for (c) and (d) three rural/remote sites, using
995 DOMINO ver. 2.0 for (a) and (c), and NASA ver. 2.1 for (b) and (d).

996

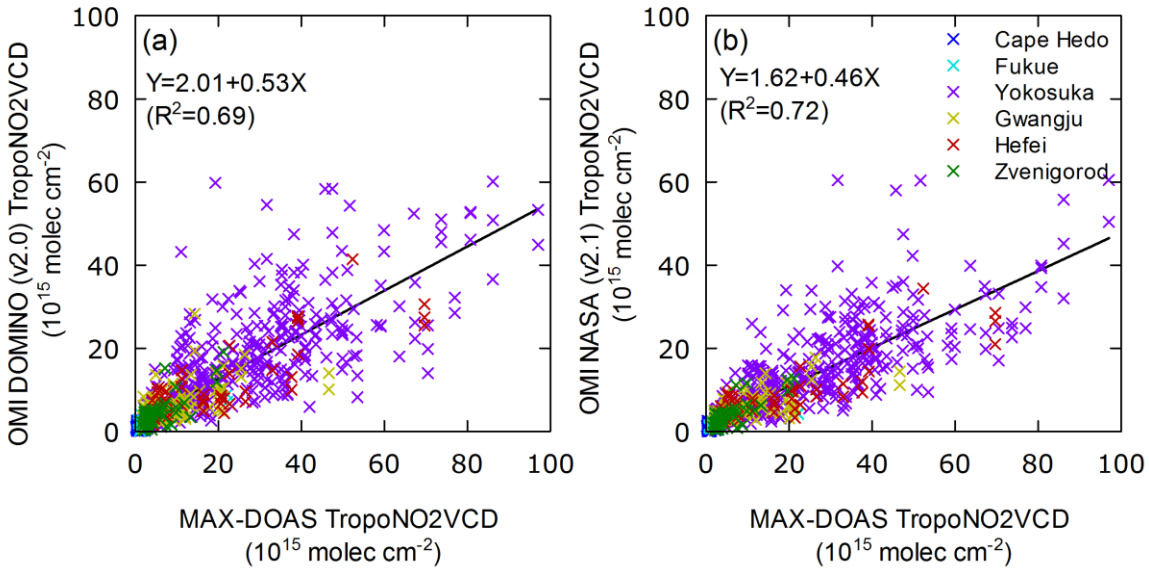

997

998 **Fig. 9.** Similar to Fig. 8 but for pixel-based comparisons with strict coincidence criteria
999 (horizontal displacement <0.15°, time difference <15 min), and cloud screening (cloud
1000 fraction <10%); DOMINO (ver. 2.0) and NASA (ver. 2.1) were used for (a) and (b),
1001 respectively.

1002

1003

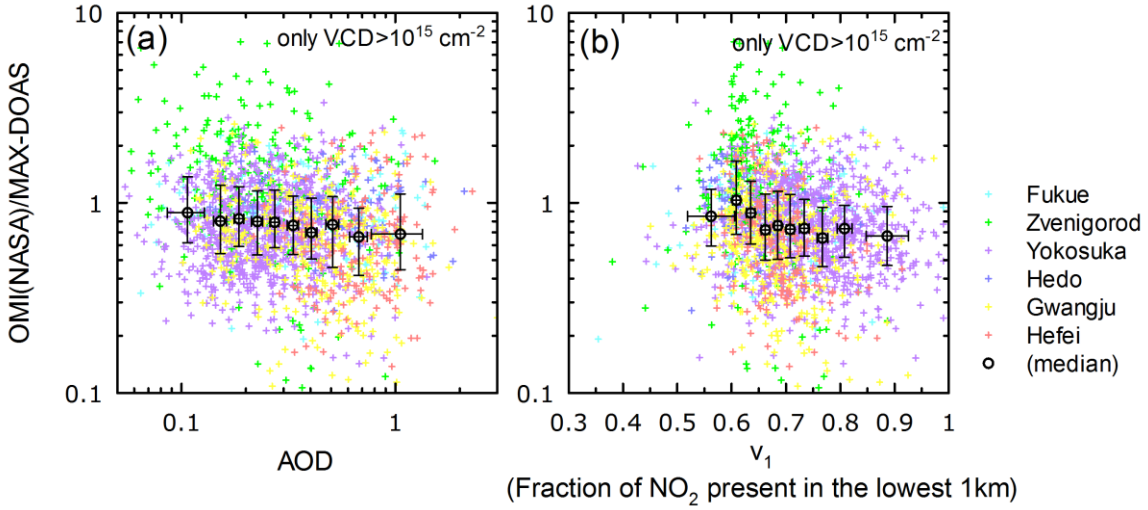

1004

1005 **Fig. 10.** OMI(NASA)/MAX-DOAS ratios for TropoNO2VCD were plotted against (a) AOD

1006 at 476 nm, observed with MAX-DOAS and (b) v_1, a retrieved parameter defining the fraction

1007 of NO_2 present in the lowest 1 km. Black circles and error bars represent the median ratios

1008 and 1σ ranges for the 10 bins sorted by AOD and v_1, respectively.

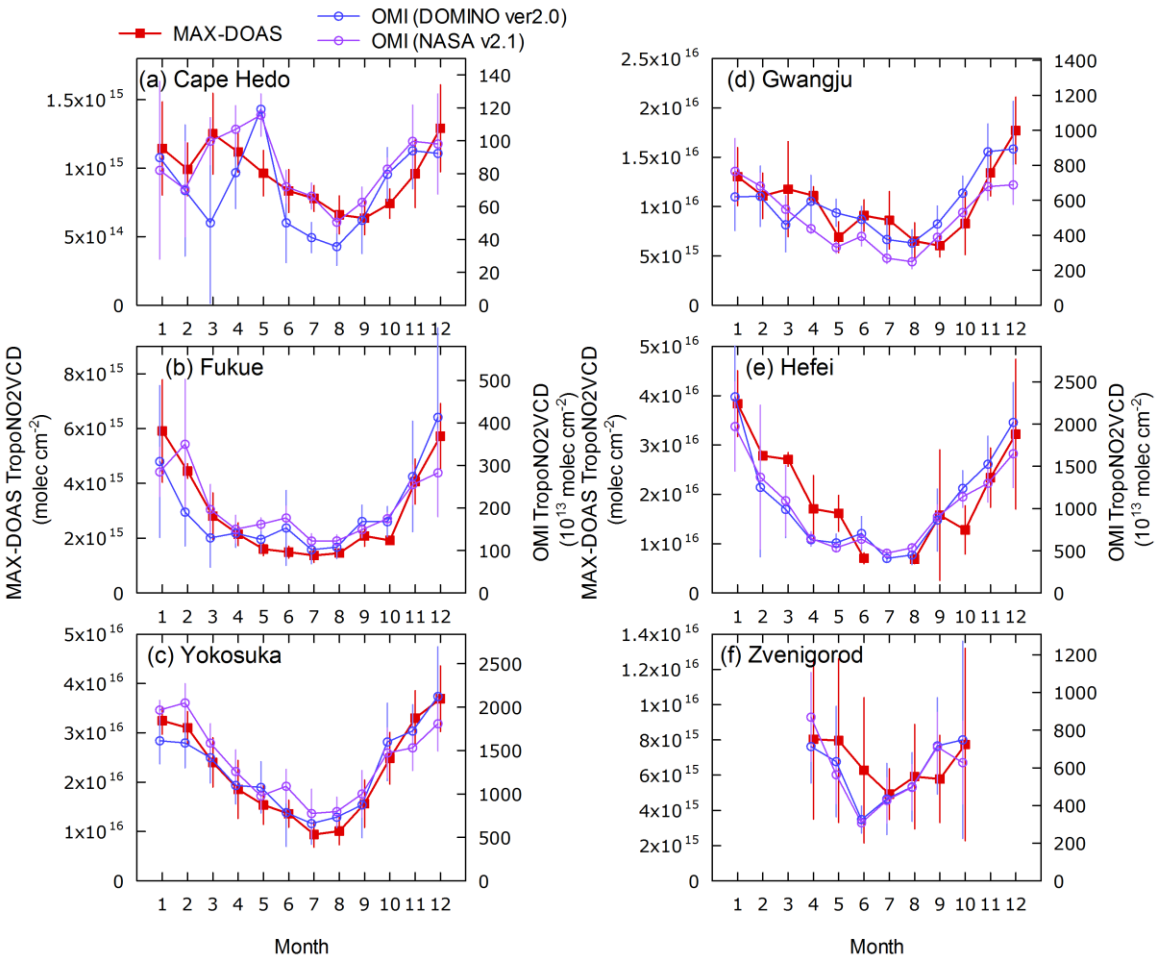

Fig. 11. Seasonality comparisons for TropoNO2VCD values derived from MAX-DOAS and satellite observations. MAX-DOAS data from the hours of satellite observations were used. The error bars represent variability in the monthly average TropoNO2VCD values over the studied years.

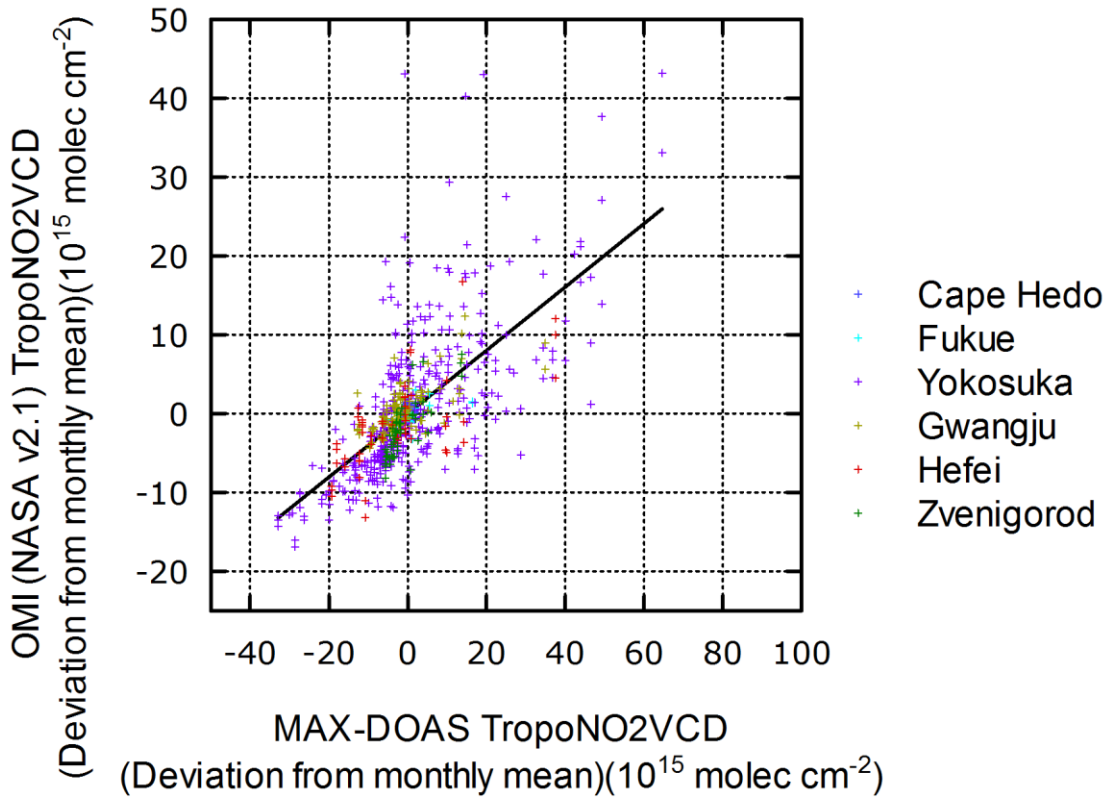

1016

1017 **Fig. 12.** Same as Fig. 9b but deviations from monthly mean values were plotted.

1018

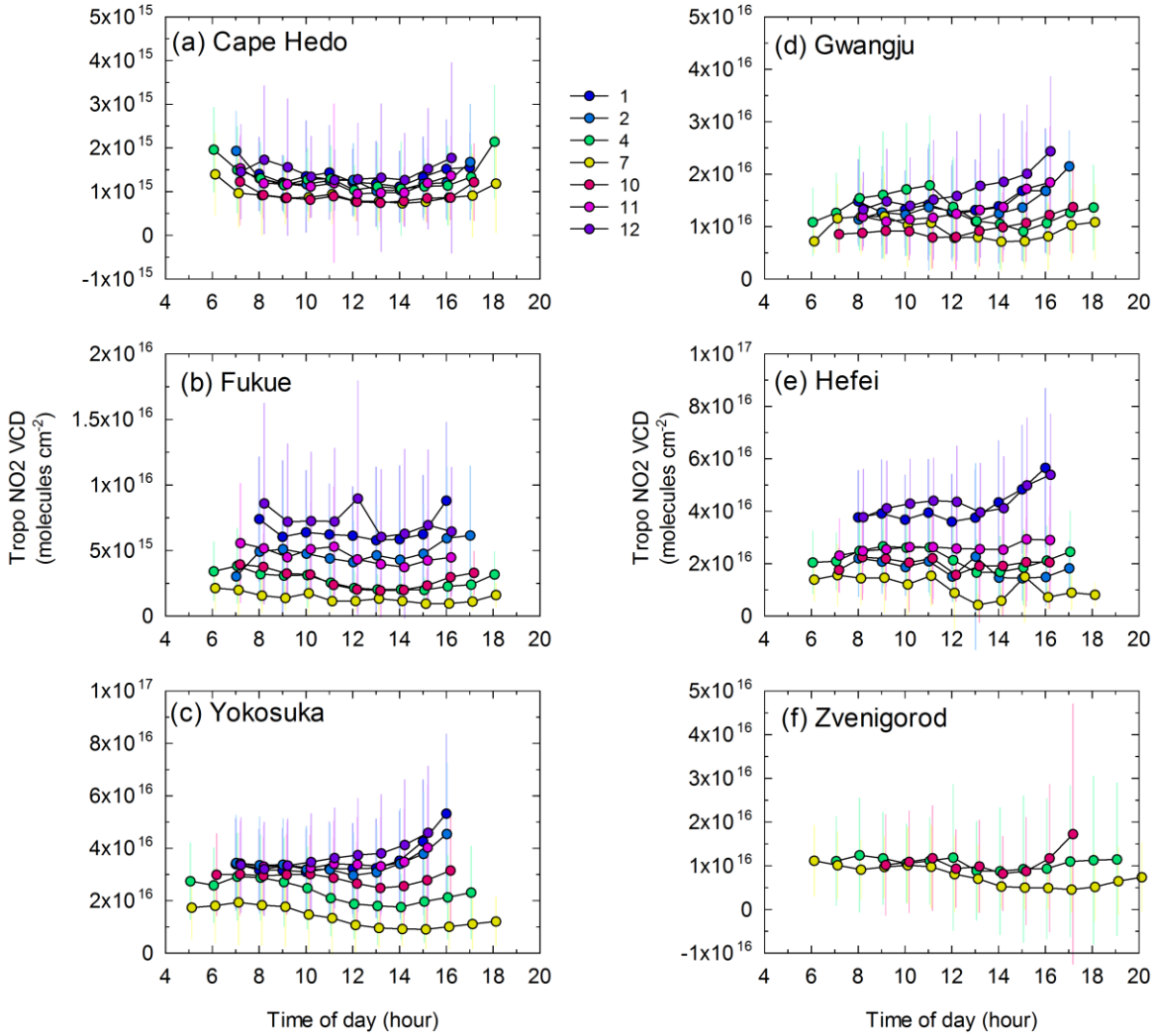

Fig. 13. Average diurnal variations in TropoNO2VCD for selected months (differently colored). Error bars represent the 1σ range of the included data.

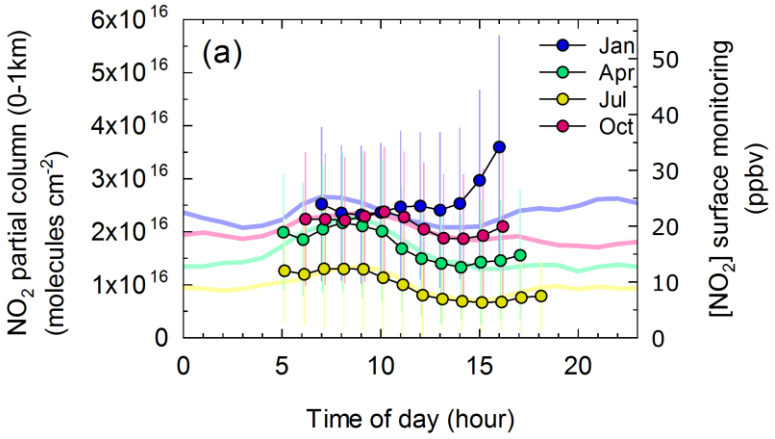

1024

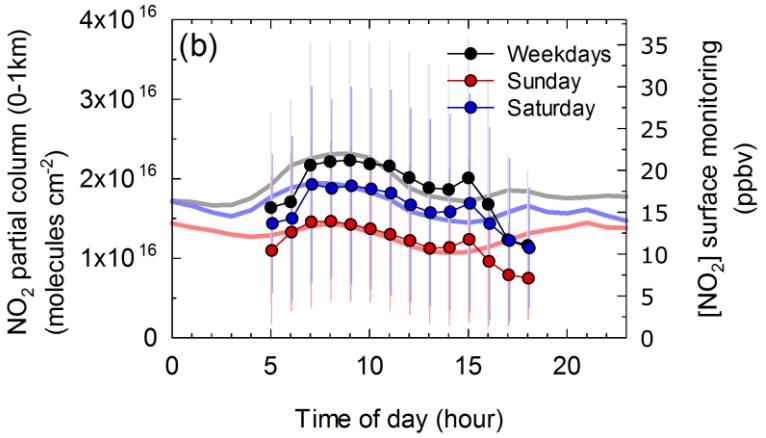

1025

1026 **Fig. 14.** Comparison of average diurnal cycles of NO_2 observed by MAX-DOAS at Yokosuka
1027 (partial columns in the lowest 1-km layer, colored circles) and by surface monitoring at
1028 Nagahama (near Yokosuka, pale colored lines) for (a) four selected months (January, April,
1029 July, and October) and for (b) weekdays and weekends. Error bars represent the 1σ range of
1030 the included data (MAX-DOAS).

1031

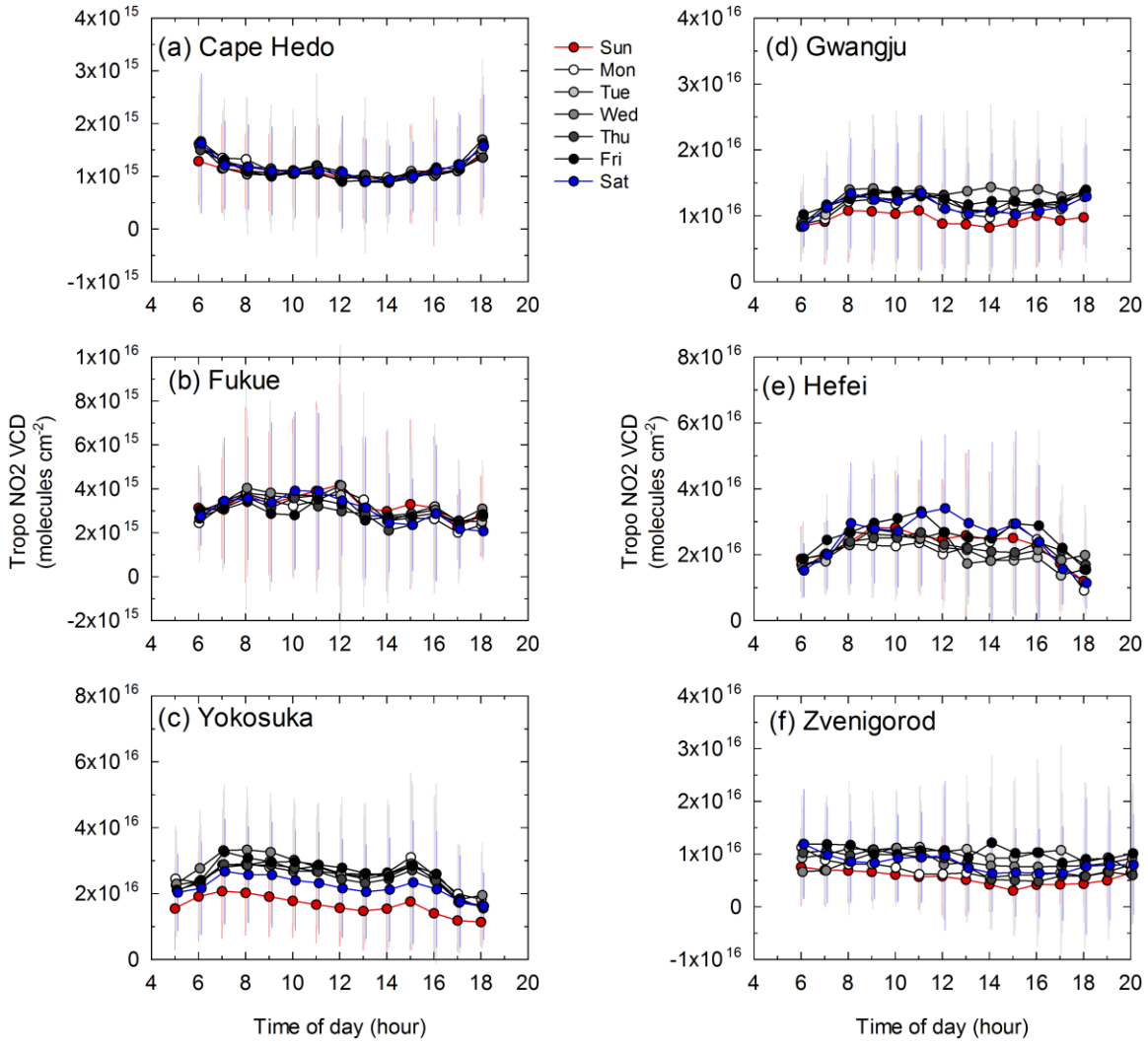

Fig. 15. Diurnal variations in TropoNO2VCD separately averaged for days of the week. Error bars represent the 1σ range of the included data.

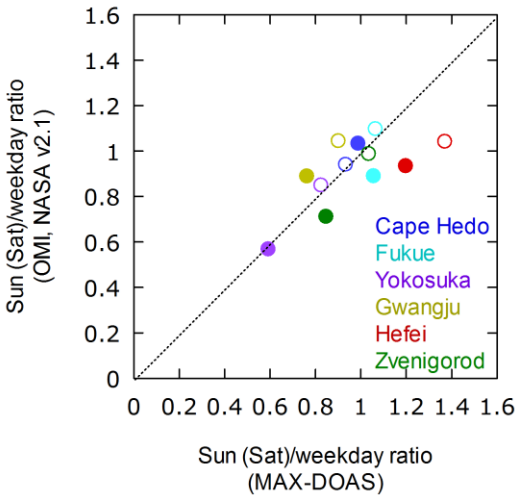

Fig. 16. Weekend reduction ratios for TropoNO2VCD derived from MAX-DOAS and OMI (using NASA ver. 2.1 algorithm). Open and closed symbol represent Saturdays and Sundays, respectively.

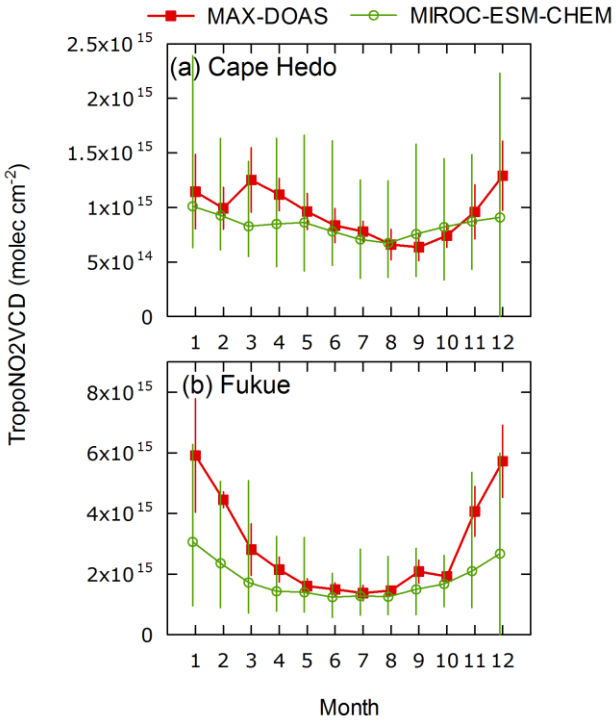

1040

1041 **Fig. 17.** Comparisons of average seasonal variations in TropoNO2VCD derived from
1042 MAX-DOAS observations and model simulations (MIROC-ESM-CHEM). Data from the
1043 hours of satellite observations (OMI) are used. Error bars for MAX-DOAS represent
1044 variations in the monthly averages over the studied years, whereas those for model
1045 simulations represent the full ranges of hourly averages included in each hour.

1046

1047

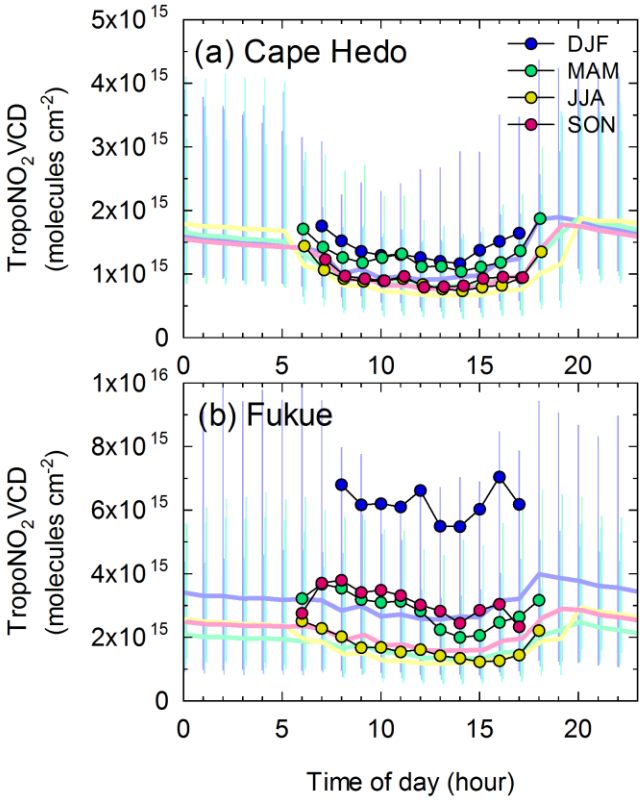

1048

1049 **Fig. 18.** Comparisons of average diurnal variations in TropoNO2VCD derived from
1050 MAX-DOAS observations (colored circles) and MIROC-ESM-CHEM model simulations
1051 (pale colored lines) for four seasons. Error bars for model simulations represent full ranges of
1052 hourly averages included in each hour.

1053

Supplementary Material

Overview and Features of AOD

The methodology used to derive AOD values at 476 nm is described in the main text, and the results are briefly summarized in this supplementary material. A color index (defined as the ratio of the intensities at 500 and 380 nm) was used to screen out cloudy cases. The threshold values used for the color index are listed in Table S1. The threshold value for Cape Hedo was changed from 1.50 (Takashima et al., 2009) to 2.40 (this study) with equivalence, because the offsets at the two wavelengths were newly taken into account for the revised calculation of the color index. For other locations, we tentatively determined the equivalent color index threshold values based on the assumption that the color ratio under conditions where the sky was the most whitish was similar to that at Cape Hedo; this provided calibration information for the relative responses of the individual instruments at 380 and 500 nm.

Figure S1 shows the time series of monthly means of the AODs at six sites, with and without cloud screening, based on the MAX-DOAS color index. The site-to-site differences were not very large in comparison with those in the case of NO_2; in particular, the AOD levels for Yokosuka (0.24 ± 0.05 (1σ) as averages of monthly mean values after cloud screening, see Table S2), an urban site, were similar to those at Cape Hedo (0.33 ± 0.13 (1σ)), a remote island. Hefei had the highest average value (0.59 ± 0.13 (1σ)) among the studied locations. The levels were roughly comparable to the climatological AOD values derived from satellite sensors, i.e., Moderate Resolution Imaging Spectroradiometer (MODIS)/Terra, MODIS/Aqua, and Multi-angle Imaging Spectroradiometer (MISR)/Terra (Fig. S1 and Table S2). The used monthly average satellite data are from MODIS/Terra (Collection 5) and MODIS/Aqua (Collection 5.1) at a $1° \times 1°$ grid resolution, and MISR/Terra (ver. 31) at a $0.5° \times 0.5°$ grid resolution, available from the NASA Goddard Earth Sciences Data and Information Services Center (http://daac.gsfc.nasa.gov/giovanni/). For the MODIS sensors, the AOD values at 550 nm were converted to those at 476 nm using the reported Ångström

parameters. For MISR, the Ångström parameters were estimated from the reported AOD values at multiple wavelengths (443, 555, 670, and 865 nm), and then the AOD values at 476 nm were estimated. Although the MODIS/Terra and MISR/Terra observations were made in the morning, and the MODIS/Aqua observations were made in the afternoon, they were all compared with the daytime averages of the MAX-DOAS observations. The AODs derived from MAX-DOAS did not show significant diurnal variations (data not shown).

Similar seasonal variation patterns at remote islands (Cape Hedo and Fukue) were found for the MAX-DOAS and satellite observations, with higher values in winter–spring as a result of long-range transport from the Asian continent along the westerlies. The agreement was excellent for Zvenigorod. Common increases in August 2010 were attributable to intense forest/peat fires. At Yokosuka, the average MAX-DOAS AOD level with cloud screening was more consistent with MISR than with MODIS (especially in summer), partly because of better spatial resolution. Similar tendencies were found for Gwangju and Hefei. For Hefei, the month-to-month variation patterns were qualitatively similar for MAX-DOAS and satellite data. Comparisons with satellite data with finer spatial resolutions will be studied in the future.

Figure S2 shows hourly-averaged AODs derived from MAX-DOAS and sky radiometer (Aoki and Fujiyoshi, 2003) data at Fukue for 2009. The AOD value at 476 nm for sky radiometer was calculated from the reported AOD value at 500 nm and the Ångstöm exponent. A strong positive correlation was found around the 1:1 line. Similar comparisons with sky radiometers and Mie lidar observations were successful at Tsukuba (Irie et al., 2008) and at Cape Hedo (Takashima et al., 2009). Based on these features, we conclude that our AOD products, with an estimated 30% uncertainty, are basically consistent with available observations. As mentioned in the main text, 30% uncertainty in the AOD introduced only 10% or less uncertainty in the TropoNO2VCD. Therefore the aerosol information can be satisfactorily used to estimate NO_2 optimally and to study the general trends in the

1106 OMI(NASA)/MAX-DOAS ratio of TropoNO2VCD against the AOD.

Table S1. Recommended threshold values for color index used for cloud screening.

Instrument	Threshold value
Cape Hedo #1	2.40
Yokosuka #1	1.67
Fukue #1	0.81
Fukue #2	2.40
Fukue #3	1.55
Gwangju #1	2.20
Gwangju #2	2.10
Gwangju #3	2.02
Hefei #1	1.74
Hefei #2	2.01
Zvenigorod #1	1.57

Table S2. Averages and 1σ ranges of monthly mean AOD values derived from MAX-DOAS observations and satellite observations.

	MAX-DOAS (with cloud screening)	MAX-DOAS (without cloud screening)	MODIS/Terra	MODIS/Aqua	MISR/Terra
Cape Hedo	0.33 ± 0.13	0.40 ± 0.14	0.26 ± 0.13	0.25 ± 0.14	0.26 ± 0.12
Yokosuka	0.24 ± 0.05	0.30 ± 0.06	0.37 ± 0.16	0.42 ± 0.18	0.27 ± 0.17
Fukue	0.29 ± 0.08	0.42 ± 0.12	0.38 ± 0.14	0.34 ± 0.12	0.37 ± 0.17
Gwangju	0.40 ± 0.10	0.50 ± 0.11	0.47 ± 0.23	0.53 ± 0.23	0.33 ± 0.18
Hefei	0.59 ± 0.13	0.73 ± 0.15	0.80 ± 0.28	0.86 ± 0.28	0.60 ± 0.23
Zvenigorod	0.21 ± 0.05	0.29 ± 0.10	0.19 ± 0.19	0.21 ± 0.22	0.18 ± 0.11

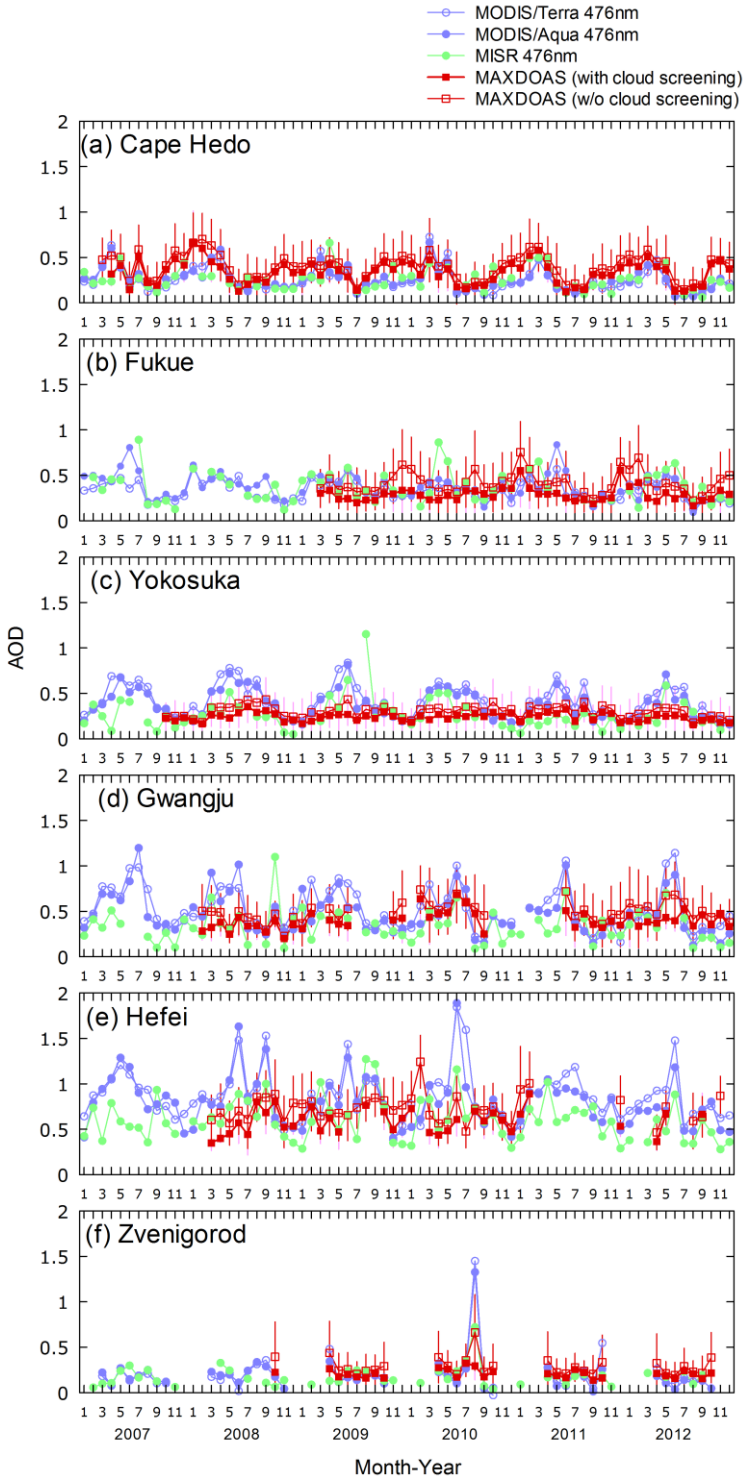

Fig. S1. Time series of monthly averages of AOD derived from MAX-DOAS and satellite observations. The satellite observations are derived using MODIS and MISR sensors on board Terra and Aqua. MAX-DOAS data, with and without cloud screening, are provided with error bars representing the 1σ range of the included data.

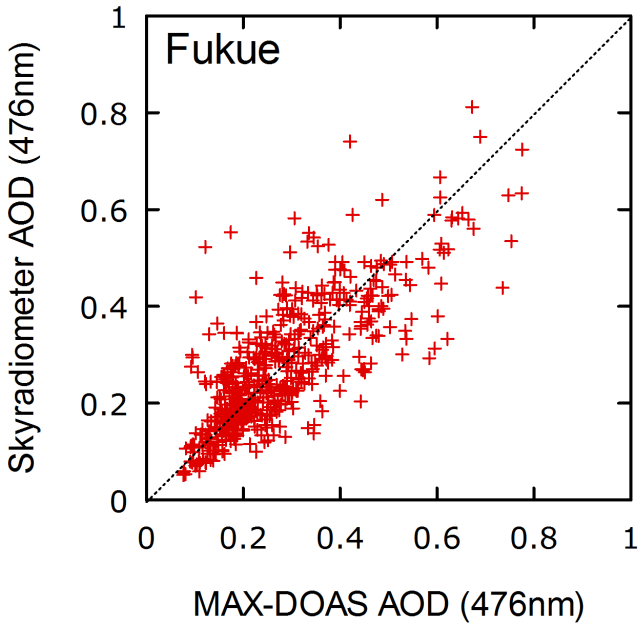

Fig. S2. Scatterplot between AODs observed by MAX-DOAS and a sky radiometer at Fukue site in 2009.

References

Aoki, K, and Fujiyoshi, Y.: Sky radiomter measurements of aerosol optical properties over Sapporo, Japan. J. Meteorol Soc. Jpn., 81, 493-513, 2003.

Irie, H., Kanaya, Y., Akimoto, H.. Iwabuchi, H., Shimizu, A., and Aoki, K.: First retrieval of tropospheric aerosol profiles using MAX-DOAS and comparison with lidar and sky radiometer measurements, Atmos. Chem. Phys., 8, 341-350, 2008.

Takashima, H., Irie, H., Kanaya, Y., Shimizu, A., Aoki, K., and Akimoto, H.: Atmospheric aerosol variations at Okinawa Island in Japan observed by MAX-DOAS using a new cloud-screening method, J. Geophys. Res., 114, D18213, doi:10.1029/2009JD011939, 2009.